이학박사 학위논문

Preclinical Internal Radiation Dosimetry Studies for Precision Radionuclide Therapy

정밀 방사성 핵종 치료를 위한 전임상 내부 흡수선량평가 연구

2023년 2월

서울대학교 융합과학기술대학원

응용바이오공학과

김 수 빈

Preclinical Internal Radiation Dosimetry Studies for Precision Radionuclide Therapy

지도교수 김 상 은

이 논문을 이학박사 학위논문으로 제출함

2023년 1월

서울대학교 융합과학기술대학원

응용바이오공학과

김 수 빈

김 수 빈의 이학박사 학위논문을 인준함

2023년 1월

위 원 장	이 원 우	(인)
부위원장	김 상 은	(인)
위 원	박 현 수	(인)
위 원	임 형 준	(인)
위 원	우 상 근	(인)

Abstract

Preclinical Internal Radiation Dosimetry Studies for Precision Radionuclide Therapy

Su Bin Kim

Department of Applied Bioengineering

Graduate School of Convergence Science and Technology

Seoul National University

Internal radiation dosimetry has become increasingly important in recent years because of the growing interest in personalized medicine and targeted radionuclide therapy (TRT). Particularly, preclinical dosimetry studies using disease model animals continue to gain interest as a promising tool for studying the biodistribution of novel theranostic radiopharmaceuticals and improving conventional radiotherapy such as “one dose fits all”. Although precise preclinical dosimetry is important to interpret dose distribution for response assessment and translate results for clinical

use, there are insufficient studies on the determination of the dosing regimen for therapeutic radiopharmaceuticals that cannot be quantitatively imaged, alpha-/beta-emitting radionuclides, and extrapolating strategies of companion diagnostic drugs.

The second chapter of this dissertation focused on the development of image-based dosimetry in xenograft mouse models. Clinically approved methods for absorbed dose estimation are recommended by the Medical Internal Radiation Dose (MIRD) Committee. Although the MIRD Committee recommended-organ level dosimetry method uses a generalized formalism for estimating the absorbed dose, the standardized geometry is not robust enough to model the size, shape, and tumor tissue heterogeneity on a subject-by-subject basis. Alternatively, voxel-level dosimetry has been developed to overcome the limitations of the conventional organ-level (or phantom-based) method, by implementing a dedicated Monte Carlo approach to simulate the complete events involved in the radioactivity decay process.

Image-based internal dosimetry at the organ-/voxel-level in the xenograft mouse model was performed using positron emission tomography/computed tomography (PET/CT) images after administering two novel diagnostic radiopharmaceuticals, [^{68}Ga]PSMA-11 and [^{18}F]PSMA-1007, via the tail vein. Voxel-level dosimetry is potentially more accurate than organ-level dosimetry for estimating doses delivered to abnormal anatomical structures, including tumor tissues. And the translated absorbed dose in humans from the xenograft model mice was compared with the reported data for prostate cancer patients. The development of accurate dosimetry strategies for these diagnostic radiopharmaceuticals could provide important insights for assessing therapeutic efficacy and interpreting the dose–response relationship during radionuclide therapy. As it is often challenging to obtain the absorbed dose

estimates for therapeutic radiopharmaceuticals, it is worth developing the voxel-level dosimetric approach for diagnostic radiopharmaceuticals that may be used as surrogates.

The third chapter of this dissertation investigates the theranostic surrogacy of companion diagnostic radiopharmaceuticals for radionuclide therapy in terms of voxel-level dosimetry. Subject-specific voxelized-phantom/-source images of differentiated thyroid cancer xenograft model mice were used, and hypothetical energy deposition maps (E_{dep}) and dose distribution maps for radioiodine–^{131}I therapy were produced from [^{123}I]NaI single photon emission computed tomography/CT (SPECT/CT). A preclinical research paradigm to advance the use of minimal scan time-point dosimetry methods has been demonstrated during TRT. After the Monte Carlo simulation, the extrapolated dose rate curves for [^{131}I]NaI were used to determine the optimal imaging scan time point of companion drugs to capture the biodistribution of therapeutic radiopharmaceuticals.

Pretherapeutic patient-specific dosimetry plays an important role in treatment planning during the TRT of various cancers to improve the probability of tumor control and reduce normal tissue toxicity. Furthermore, preclinical internal radiation dosimetry is valuable in terms of translational research to optimize dose-finding and assessment of therapeutic efficacy. The direct Monte Carlo simulation approaches employed in this dissertation provided a fundamental basis for managing the therapeutic strategies for promising radiopharmaceuticals and improving patient-specific treatment plans.

Keywords: Preclinical internal radiation dosimetry, Monte Carlo simulation,

Targeted radionuclide therapy, Personalized medicine, Theranostics

***Student number*:** 2019-25365

Contents

Figure legends

Table legends

Chapter 1. Introduction

Internal radiation dosimetry has become increasingly important in recent years because of the growing interest in targeted radionuclide therapy (TRT) and personalized medicine. TRT finds the specific target and delivers ionizing radiation to that target to inhibit its function [1], which is aiming to maximize the highest possible therapeutic efficacy for the tumor while sparing healthy tissues to diminish toxicity.

Preclinical evaluation of novel diagnostic or theranostic radiopharmaceuticals in disease/target-specific xenograft animal models is gaining interest because evident-based clinical dose selection, the dose–response relationships, and safety in terms of internal radiation dosimetry must be translated before these radiopharmaceuticals can be implemented as personalized medicine and TRT for patients [2,3]. Particularly, during multiple cycles of TRT, dosimetry-guided response assessment is essential not only for formulating the therapy plans and post-treatment but can be used as the fundamental basis for describing the surrogacy for TRT.

Patient-specific image-based dosimetry involves the patient's own anatomical information and spatial distribution of radioactivity over time [4,5]. The physical properties of radionuclides from internal sources, pharmacokinetics, and anatomical organ geometry determine the absorbed dose. Clinically approved methods for absorbed dose estimation are recommended by the Medical Internal Radiation Dose (MIRD) Committee [6]. The absorbed dose ($\mathrm{D}(r_t, T_D)$) was calculated with S values of each radionuclide for the source–target organ pairs and time-integrated activity coefficients ($\tilde{A}$) [7,8]:

$\mathrm{D}(r_t, T_D) = \sum_{r_s} \int_0^{T_D} \tilde{A}\,(r_s, T_D)\ \ S(r_T \leftarrow r_s)dt$, where r_t is the target organ, and $\tilde{A}(r_s, T_D)$ is the time-integrated activity in source organ r_s over the dose integration period T_D.

Although the MIRD method uses a generalized formalism for estimating the absorbed dose, this approach does not incorporate patient-specific activity distributions and organ anatomies. Because the standardized geometry is not robust enough to model the size, shape, and location of every unique tumor discovered in patients

Alternatively, voxel-based dosimetry, which implements the Monte Carlo approach to simulate the complete events engaged in the radioactivity decay process, is considered potentially more accurate than the MIRD method because it considers activity distributions, organ anatomies, and tumor tissue heterogeneity on a subject-by-subject basis [2,9]. The absorbed dose calculation as follows: $\mathrm{D}(voxel_k) = \sum_{h=0}^{N} \tilde{A}voxel_h \cdot S(\,voxel_k \leftarrow voxel_h)$

Many MC radiation transport codes and dosimetry platforms, such as EGSnrc, MCNPx, Geant4/Geant 4 Application for Tomographic Emission (GATE), and RAPID (Radionuclide Assessment Platform for Internal Dosimetry), were developed for clinical/preclinical voxel-level dosimetry studies [2,10–15]. The trajectories of the particles originate at the specific voxel and the destination is a random voxel. The example of voxel-level absorbed dose estimation step by dosimetry platforms, GATE MC simulation, is illustrated in **Figure 1.1**.

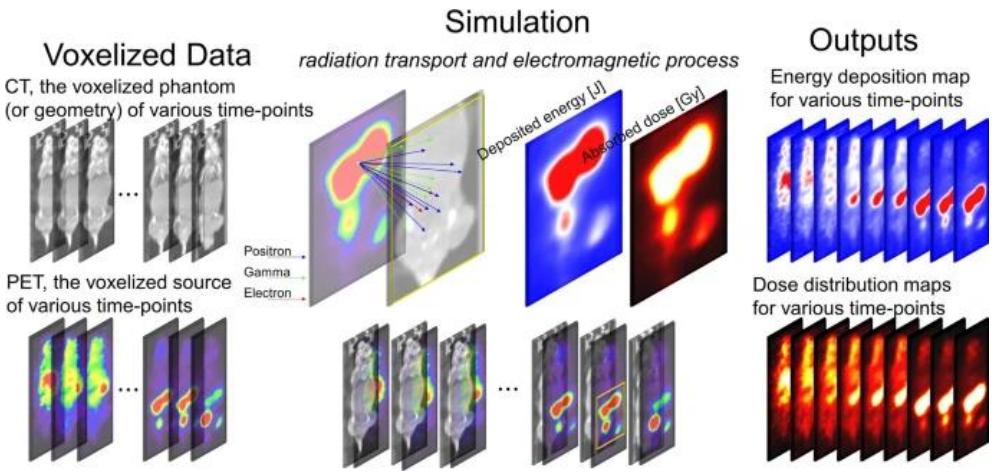

Figure 1.1 Graphical diagram illustrating how a dose map is generated. GATE simulates electromagnetic physical processes according to radioactive decay.

Theranostics is a paradigm in which the pairing of molecular imaging with therapy. Several diagnostic-/therapeutic radiopharmaceuticals have gained increasing importance to selectively detect and treat targets for various cancers, such as neuroendocrine tumors, prostate cancer, and lymphoma [16–18]. Miller et al. classified the class of theranostic pairs; same-element isotope pairs, different-element pairs, and different-pharmaceutical pairs according to the element of chemical, given isotope, the pharmaceutical, and/or the chelator [19]. However, several therapeutic radionuclides are challenging to obtain quantitative images due to low injected activities or low positron emission. In terms of theranostics, theranostic pairs have been investigated to overcome the limitations of imaging for therapeutic radionuclides and the application using surrogacy has been developed for a variety of cancers/diseases [20].

A series of quantitative scans over multiple days for each therapy and time-consuming processing/calculation make it difficult to perform personalized dosimetry in clinical. To improve these challenges, a variety of simplified approaches including single time point (STP) dosimetry to enable routinely have been developed for personalized TRT by using single scan acquisition [21–25]. These simplified dosimetry strategies have been anticipated to improve patient comfort and reduce economic costs [26].

Research objectives

The goal of this research is to demonstrate a preclinical research paradigm to advance the use of voxel-level dosimetry in TRT to deliver personalized dosimetry considering patient-specific heterogeneous tissue compositions and activity distribution.

In Chapter 2, the image-based internal radiation dosimetry for various organs, including tumors, was developed in a subcutaneous prostate cancer xenograft model mice. As preclinical dosimetry could be applied to determine the dose of TRT for cancer patients, xenograft model mice were generated by human prostate cancer cells (22Rv1, [^{68}Ga]PSMA-11; LNCaP, [^{18}F]PSMA-1007). With well-established prostate cancer diagnostic radiopharmaceuticals with high specificity, PET/CT images were deployed to estimate absorbed dose at both organ-/voxel-level dosimetry respectively. At the organ-level, MIRD-recommended absorbed dose calculation was used, and a dedicated dosimetry platform, GATE Monte Carlo simulation, was applied as voxel-level absorbed dose calculation. Finally, the ability of voxel-level dosimetry was demonstrated compared to the conventional organ-level method and provided a fundamental basis for the use of voxel-level dosimetry in TRT considering patient-specific heterogeneous tissue compositions and activity distributions. As the image-based voxel level dosimetry method for diagnostic radiopharmaceuticals produced more realistic voxel level dose distribution, these dosimetric strategies could be expanded for radionuclide therapy. The voxel-level absorbed dose estimates for therapeutic radiopharmaceuticals in a xenograft mouse model were applied with surrogates—the same element theranostic pairs.

In Chapter 3, the theranostic surrogacy of companion diagnostic radiopharmaceuticals in differentiated thyroid cancer (DTC) xenograft mouse model was investigated in terms of voxel-level dosimetry. ^{123}I and ^{131}I have been used for a long time as same-element isotope theranostic pairs for thyroid disease treatment and their biological behaviors were assumed to be identical. The DTC xenograft mouse models were generated after validating iodine uptakes via NIS proteins through in vitro assays. Although ^{131}I imaging was less quantitative for producing three-dimensional dose distribution, [^{123}I]NaI SPECT/CT images up to 64 h were used as voxelized phantoms and voxelized sources for dedicated Monte Carlo simulation. The absorbed dose per unit injected dose was calculated for the DTC disease model and could be described as the surrogacy for radioiodine therapy. Meanwhile, the pretherapeutic dose determination for DTC therapy was controversial because of unsatisfactory accuracy and demanding process. The minimal scan time point dosimetry for various TRT has been developed to overcome the issues and has been investigated whether applicable or not in a clinical environment. Finally, the simplified approach at the voxel-level was proposed for tumor absorbed dose and DE was calculated comparing to data up to 64 h.

Chapter 2. The development of image-based dosimetry in the xenograft model mice: Application for prostate cancer diagnostic radiopharmaceuticals

2.1 Background

Prostate-specific membrane antigen (PSMA) is a cell surface protein that exhibits a significantly increased expression in prostate cancer cells, which makes it ideally suited for molecular imaging [27]. Having demonstrated remarkable affinity to PSMA in numerous trials, [^{68}Ga]PSMA-11(*N*,*N'*-bis[2-hydroxy-5-(ethylene-b-carboxy)benzyl]ethylenediamine-*N*,*N*'-diacetic acid (HBED-CC)) and [^{18}F]PMSA-1007((((3S,10S,14S)-1-(4-(((S)-4-carboxy-2-((S)-4-carboxy-2-(6-^{18}F-fluoronicotinamido)butanamido)butanamido)methyl)phenyl)-3-(naphthalen-2-ylmethyl)-1,4,12-trioxo-2,5,11,13-tetraazahexadecane-10,14,16-tricarboxylic acid))) have been adopted for clinical use at several institutions worldwide. And they have become established as the most widely used diagnostic radiopharmaceutical for positron emission tomography (PET) in clinical practice [28–33].

The use of PSMA-targeting radiopharmaceuticals for companion diagnostics has gained significant attention during the last decade, various PSMA-targeting radioligands that can be labeled with alpha- (e.g., actinium-225) and beta-emitting radionuclide (e.g., lutetium-177 and yttrium-90) have been developed for therapeutic use. In terms of companion diagnostics, these promising diagnostic radiopharmaceuticals have been widely demonstrated to be a useful component as a

predictor of the response to therapeutic treatment as well as diagnosis of prostate cancer [34–36].

Although the application of [^{68}Ga]PSMA-11 and [^{18}F]PSMA-1007 PET coupled with therapeutic radiopharmaceuticals is currently under broad clinical and scientific investigation, insufficient preclinical studies have been performed to determine the dosing regimen for the therapeutic radiopharmaceuticals.

At the organ-level, the mean absorbed dose (D) in the target organ (r_t) was calculated using the time-integrated activity ($\tilde{A}$) in the source organs (r_S) obtained from the PET image-based biodistribution data and the S-values ($\mathrm{S}(r_t \leftarrow r_s)$). Furthermore, voxel-based method for estimating the absorbed dose was performed by applying the GATE Monte Carlo simulation. GATE is based on the Geant4 toolkit [37], which is a well-established code for radiation transport. All simulations in this study used GATE version 9.0, which has been extended for dosimetry applications. As such, GATE has been used primarily for studies focused on nuclear medicine imaging, radiation therapy, and dosimetry applications providing personalized dosimetry for TRT [3,38–42]. Specifically, GATE contains a mechanism, named *DoseActor*, which stores the absorbed dose in a given volume in a 3D matrix [43]. (where r_t is the target organ, and $\tilde{A}(r_s, T_D)$ is the time-integrated activity in source organ r_s over the dose integration period T_D.)

The anatomical difference in the small-sized standardized models, significantly affects the variation in the absorbed dose and makes a difficult to develop personalized dosimetry. So several preclinical dosimetry studies concluded that specific digital mouse models could not be applied for personalized murine dosimetry studies [44,45].

The Monte Carlo simulation successfully generated the corresponding dose distribution maps for each voxelized source—i.e., the PET and/or SPECT images (uncorrected for radiation decay) of every time-point, which represent the amount of radioactive decay at a given time-point in the simulation of the interaction between particles and materials—against the voxelized phantom—i.e., the CT images of every time-point, which represent materials such as air, air-body interface, soft tissue, and bone that were segmented according to the threshold of the Hounsfield unit values used in the simulation—of each individual model mouse. The E_{dep} maps and Dose maps were produced using subject-specific PET/CT and/or SPECT/CT images as input data, and a subject-/organ-specific dose rate curve was produced.

2.2 Experimental

2.2.1 General experimental section

Generation of xenograft model mice.

The mice were housed in a pathogen-free room maintained at ~21°C, ~55% relative humidity, and a 12 h light/dark cycle, with food and water available ad libitum. Feeding was limited prior to PET/CT imaging. All tumor-bearing mice whose tumor sizes were measured using the formula: tumor size (cm^3) = (width (cm^2) × length (cm))/2.

All animal experiments were carried out in accordance with the approved guidelines. The study is compliant with the ARRIVE guidelines. All animal experimental protocols were approved by the Institutional Animal Care and Use Committee (IACUC) of Seoul National University Bundang Hospital, Seongnam, Korea.

Image analysis and quantification

The tumor-bearing mice underwent an animal-dedicated PET/CT system (NanoPET/CT, Mediso Inc., Budapest, Hungary). The mice were maintained under 2% isoflurane anesthesia during PET/CT scanning. The dynamic image frames were reconstructed using the iterative three-dimensional ordered subset expectation maximization (OSEM) algorithm and the single-slice rebinning (SSRB) method. During image reconstruction, attenuation corrections were applied for CT-related scatter and decay. The reconstructed images had a volume of 142 × 142 × 163 mm^3 and a voxel volume of 0.6 × 0.6 × 0.6 mm^3.

The PET image-based biodistribution data obtained from the organs were plotted as a function of time to generate time activity curves (TACs). For each organ, the measured activity (in kBq/cc) was normalized to the total injected activity to express the percentage of injected dose per gram (%ID/g). The number of voxels within the VOIs drawn for an organ at each time point was averaged and multiplied by the voxel volume and tissue density to estimate the organ mass.

The pharmacokinetic parameters in each organ were assessed quantitatively using the TACs of the organs of interest: peak concentration (C_{max}), time to reach C_{max} (T_{max}), half-life ($T_{1/2}$), and area under the TAC (AUC).

Voxel-level dosimetry method

A well-established code for radiation transport, GATE was performed for estimating voxel-based absorbed dose. The CT and PET images of the mice were resampled at the same voxel dimensions and used as the voxelized phantom and voxelized source, respectively, representing the inputs to GATE for the dosimetry simulations. For each PET frame, a separate simulation was run based on the corresponding biodistribution data and PET frame durations. The *DoseActor* mechanism stores the absorbed dose in a given volume in a 3D matrix and the *ImageRegularParametrisedVolume* option was applied for the simulation of a voxelized phantom using the CT image of a real mouse [43].

The ^{68}Ga and/or ^{18}F ion-source type from Geant4 version 10.6 was used for the simulation. The standard electromagnetic physics package of GATE, which includes the photoelectric effect, Compton scattering, bremsstrahlung radiation, and positron–electron used for all simulations. And the simulation was run using the

Mersenne Twister (Matsumoto and Nishimura 1998) random number generator [46]. The voxel-level statistical uncertainties were kept below 2% [9]. Before conducting the GATE Monte Carlo simulation, validation studies to evaluate the performance were performed. The simulation was run on an in-house computing cluster with a 32-core CPU and 64 GB RAM.

The simulation outputs the energy deposition (E_{dep}) map, dose distribution map, number of hits, and the local statistical uncertainty. Using the *DoseActor* mechanism, the deposited energy (in MeV) in the voxels within the VOIs drawn over each organ was estimated. Subsequently, the absorbed doses in the voxels were calculated by dividing the deposited energy in each voxel by the voxel mass. Finally, the voxel doses within the VOIs were summed to obtain the absorbed dose for the entire organ. Then, the dose rate (in Gy/s) for each organ from the PET frame was calculated by dividing the absorbed dose by the respective simulation time. The AUC of each dose-rate curve was calculated as the trapezoidal sum of the observed data and extrapolated to infinity by integrating the effective decay for the curve tail. The voxel-level absorbed dose estimation was normalized to the activity of the injected dose for each mouse.

Organ-level dosimetry method

The S-values of the ^{68}Ga and ^{18}F radioisotope for the source–target organ pairs were taken from the database published to calculate the absorbed dose in each organ [12]. To provide organ-level absorbed dose estimates in abnormal organs (e.g., tumors) without published S-values, an alternative approach embedded in the IDAC/Dose2.1 software was attempted to estimate the absorbed dose [47]. A previous study

addressed a similar limitation in estimating a patient's dosimetry using the sphere model of OLINDA 1.1 [31,48,49]. It assumed that the tumor is a sphere of uniform density and that the distribution of the radiopharmaceutical in the abnormal organ is homogeneous regardless of its shape, location, and target density. The tumor density, tumor volume, and residence time for the real xenograft mice were used as inputs in the IDAC Spheres sub-module involved in the software for adult reference voxel phantoms [8].

Dosimetry Prediction for Clinical Translation

The human residence time from our xenograft model mice was proposed by Constantinescu et al [50–52]. The organ and whole-body weight difference between species was used for normalization and IDAC-Dose 2.1 software calculated the human effective dose [51–53]. The human normalized residence times of each radiotracer were obtained from the product of the preclinical residence time of a compartment and a scaling factor, with the latter calculated using $(B_r / O_r) \times (O_h / B_h)$ [54], where B_r and B_h are the body masses and O_r and O_h are the individual organ masses for mice and humans, respectively.

Graphical and statistical analysis

All graphs and statistical analyses were generated using GraphPad Prism 8.0. All quantitative data are expressed as the mean ± the standard error of the mean (SEM). The statistical significance was analyzed using the independent *t*-test. Differences with a *P*-value less than 0.05 were considered statistically significant.

2.2.2 [^{68}Ga]PSMA-11

Experimental xenograft model mice

Male BALB/c mice (6 weeks old) were purchased from Orient Bio (South Korea). PSMA-positive (22Rv1) human prostate carcinoma cell lines were purchased from American Type Culture Collection (Rockville, MD, USA). All experimental model mice were generated in-house. Six of the mice had 22Rv1 tumors, which were induced by inoculating 22Rv1 PSMA-positive cells (1.0×10^7 cells in 100 μL phosphate-buffered saline) into the right flank of each mouse, and three of mice bearing both 22Rv1 and PC2 PSMA-negative cells (1.0×10^7 cells in 100 μL phosphate-buffered saline) were used to investigate the selectivity.

Preparation of [^{68}Ga]PSMA-11

$^{68}Ga^{3+}$ obtained from a $^{68}Ge/^{68}Ga$ radionuclide generator (iThemba LABS, Somerset West, South Africa) was used for the radiolabeling of PSMA-11. The precursor peptides (1 nmol in 0.1 M HEPES buffer, pH 7.5, 90 μL) were added, in a volume of 100 μL, to a mixture comprising 10 μL of 2.1 M HEPES solution and 10 μL of [^{68}Ga]Ga^{3+} eluate (50 –100 MBq). Next, the pH of the labeling solution was adjusted to 4.2. Then, the reaction mixture was incubated at 80°C for 2 min. The radiochemical yield was determined using high-performance liquid chromatography (HPLC). This approach achieved typical radiochemical yields of $52.07 \pm 1.42\%$ (non-decay corrected) and radiochemical purity > 99%.

Whole-body dynamic PET imaging was performed over a duration of 90 min immediately after administering an intravenous injection of [^{68}Ga]PSMA-11

(3.10 ± 0.13 MBq) to each mouse via a catheter inserted in its tail vein. In addition, PET/CT images at 3, 4, and 5 h after [^{68}Ga]PSMA-11 administration were acquired.

Image analysis and quantification

[^{68}Ga]PSMA-11 to correct for the activity concentration (Bq/ml) in the reconstructed PET images. The VOIs were drawn manually over the major organs (tumor, heart, lungs, kidneys, liver, bladder wall, and intestine) on the CT and time-integrated PET images using PMOD software (version 3.6, PMOD Technologies Ltd., Zurich, Switzerland), taking care to ensure that the VOIs did not overlap. The pharmacokinetic parameters were calculated using GraphPad Prism software (version 8.0, GraphPad Software, La Jolla, CA, USA).

To examine the selectivity by demonstrating the greater uptake of [^{68}Ga]PSMA-11 in the PSMA-positive (22Rv1) tumor compared to the PSMA-negative (PC3) tumor, three model mice bearing both 22Rv1 and PC3 tumors were underwent a static 20-min PET/CT study 90 min after the intravenous injection of [^{68}Ga]PSMA-11 (2.20 ± 0.38 MBq).

To investigate the specificity by demonstrating the inhibited uptake of [^{68}Ga]PSMA-11 in the PSMA-positive (22Rv1) tumor after treatment with the potent and selective inhibitor 2-PMPA (2-(Phosphonomethyl)-pentanedioic acid) of glutamate carboxypeptidase II30, the three 22Rv1 tumor-bearing mice before and after 2-PMPA treatment. The mice underwent static 20-min PET/CT studies 90 min after the intravenous injection of [^{68}Ga]PSMA-11 (before: 3.10 ± 0.13 MBq; after: 2.87 ± 0.04 MBq).

2.2.3 [^{18}F]PSMA-1007

Experimental xenograft model mice

Male BALB/c mice (*n* = 8, 6 weeks old) were purchased from Orient Bio (South Korea). A PSMA-positive human prostate carcinoma (LNCaP, Lymph node carcinoma of the prostate) cell line was purchased from Korea Cell Line Bank (South Korea) and maintained in RPMI 1640 medium containing 10% fetal bovine serum. LNCaP cells (1.0×10^7 cells in 200 μL phosphate-buffered saline) were inoculated subcutaneously into the right flank of the mouse. The whole-body PET/CT images of the eight LNCaP tumor-bearing mice at 0–120 min (dynamic) post-injection of [^{18}F]PSMA-1007. The other five LNCaP tumor-bearing mice who were assigned to the inhibition group in the specificity study underwent 120-min dynamic whole-body PET/CT scans after treatment with the PSMA-selective inhibitor.

Preparation of [^{18}F]PSMA-1007

The radiolabeling precursor (PSMA precursor, acetate salt) was obtained from ABX Advanced Biochemical Compounds [34,36]. [^{18}F]PSMA-1007 was produced according to the known method by adapting solid phase extraction (SPE) and high-performance liquid chromatography (HPLC) purification [55]. In this study, the commercial sCUBE radiosynthesizer (FutureChem, South Korea) was used to produce [^{18}F]PSMA-1007 in high radiochemical yield (RCY) with the HPLC purification system. The overall synthesis time was approximately 55 minutes (including HPLC purification), and the isolated RCY was in the range of 30–32% (*n* = 25, non-decay corrected). Quality control (QC) of [^{18}F]PSMA-1007 satisfied nine release criteria (i.e., appearance, identity, radiochemical purity, radionuclidic purity,

chemical purity, pH, endotoxins, filter integrity, and sterility). All QC parameters were determined to be within the acceptable criteria, and there were no outstanding deviations [56].

Image analysis and quantification

The volume of interest (VOI) was drawn manually over the major organs (tumor, salivary glands, heart, lungs, kidneys, liver, intestine, and urinary bladder) on the fused PET and CT images, taking care to ensure that the VOIs did not overlap. The number of voxels within the VOIs drawn for an organ at each time point was averaged and multiplied by the voxel volume and tissue density to estimate the organ mass. The [^{18}F]PSMA-1007 uptake for each organ was estimated for each mouse by applying VOIs over the respective organs on the PET images. The PET image-based biodistribution data obtained from the organs were plotted as a function of time to generate time-activity curves (TACs). For each organ, the measured activity (in kBq/cc) was normalized to the total injected activity to express the percentage of injected dose per gram (%ID/g). The pharmacokinetic parameters of [^{18}F]PSMA-1007 in each organ were evaluated quantitatively using the TACs of the organs of interest: peak concentration (C_{max}), time to reach C_{max} (T_{max}), half-life ($T_{1/2}$), and area under the TAC (AUC). The pharmacokinetic parameters were calculated using PK and PKNCA R packages [57,58]. In estimating $T1_{/2}$, a bi-exponential function was used to fit the lung, heart, and liver data, and a mono-exponential function was used to fit the salivary gland and intestinal data to the last three time points.

Kinetic Analysis with an Irreversible Two-tissue Compartment Model and the Image-derived Input Function

For the subsequent repeatability and specificity analysis described below, a kinetic analysis was performed to quantify the in vivo tumor binding characteristics of [^{18}F]PSMA-1007 involving a plasma compartment (C_P), free and non-specifically bound component in the tissue compartment (C_{NS}), and the target-specific compartment (Cs). An irreversible two-tissue compartment model (2T3k) was used with rate constants K_1, k_2, and k_3 [34,59,60], where K_1 and k_2 are forward and reverse transport coefficients, respectively, between the C_P and C_{NS}; k_3 represents the association of a tracer binding to the active site of the target and being internalized, i.e., Cs. In the model, the tracer was not considered to dissociate from the zinc active site of PSMA and be externalized. The time course (TAC) of [^{18}F]PSMA-1007 in the left ventricle (the image-derived input function, as C_P) and the tumor (as C_{NS}+Cs) were fitted to the model to estimate K_1, k_2, and k_3. Then, the net influx rate constant was calculated as follows: $K_i = (K_1 \times k_3) / (k_2 + k_3)$

Repeatability and Specificity

Repeatability of the uptake of [^{18}F]PSMA-1007 was tested using datasets of separately acquired 120-min dynamic whole-body PET/CT scans, Scan 1 and Scan 2, respectively, in the same animals. The uptake of [^{18}F]PSMA-1007 was normalized in the standardized uptake value (SUV) rather than %ID/g to follow the unit of the diagnostic clinical convention. TAC of [^{18}F]PSMA-1007 in the tumor was mainly used in this analysis. Repeatability was assessed by relative difference (D), a within-subject coefficient of variation (wCV), repeatability coefficient (RC), and intraclass

correlation coefficient (ICC) [61]. The relative difference in SUV between scans was calculated as $(SUV_{scan\ 1} - SUV_{scan\ 2}) / ([SUV_{scan\ 1} + SUV_{scan\ 2}] / 2) \times 100\%$. The wCV was calculated as the standard deviation (SD) of the relative differences over all subjects divided by $\sqrt{2}$. The RC is a threshold value within which 95% of the normal variability between measurements occurs and was calculated using symmetric limits as $1.96 \times \sqrt{2} \times$ wCV. ICC was estimated using a one-way model as for each animal, two PET images were taken.

The specificity of the uptake of [^{18}F]PSMA-1007 was investigated *via* group comparison analysis. The inhibition group consisted of five LNCaP tumor-bearing mice who underwent 120-min dynamic whole-body PET/CT scans preceded by PSMA-selective inhibitor 2-PMPA (50 mg/kg) treatment [62], and the data for the baseline group was the 120-min dynamic whole-body PET/CT images acquired for biodistribution and pharmacokinetics. The activity measured in the prostate tumor of each mouse was normalized to the total injected dose of each radiopharmaceutical and divided by the mass of the respective tumors to obtain the SUV. The SUV as a function of time was plotted to generate TACs and compared the AUCs.

The differences between Scan 1 and Scan 2, and the rate constants (K_1, k_2, k_3, and K_i) between before and after 2-PMPA treatment were also compared by independent *t*-test with a $P < 0.05$ indicating statistical significance.

2.3 Results

2.3.1 [^{68}Ga]PSMA-11

Biodistribution and pharmacokinetic

Figure 2.1 and **Figure 2.2** shows the biodistribution and clearance of [^{68}Ga]PSMA-11 for PSMA-positive tumor (22Rv1)-bearing mice after intravenous injection. The **Figure 2.1** illustrates rapid whole-body distribution immediately after the injection, followed by rapid washout (at variable rates) for peripheral organs, including the liver, whereas other organs, namely the kidneys, urinary bladder, and the tumor, demonstrated a longer lasting substantial uptake of [^{68}Ga]PSMA-11. The kidneys and urinary bladder showed substantial accumulation of [^{68}Ga]PSMA-11 without exhibiting a washout phase during the period of the study. The kidneys showed the highest accumulation of [^{68}Ga]PSMA-11 without exhibiting a washout phase during the study. The urinary bladder was the predominant excretion route of the intravenous injection of [^{68}Ga]PSMA-11 with twofold greater accumulation than the intestine. The pharmacokinetic parameters for the visualized organs and the tumor are summarized in **Table 2.1**. The tumor exhibited a peak [^{68}Ga]PSMA-11 concentration of 4.5 ± 0.7%ID/g 2 h (on average) after the injection, which decreased gradually thereafter, measuring approximately 3%ID/g after 5 h.

Additionally, the pharmacokinetics of [^{68}Ga]PSMA-11 were characterized in terms of selectivity and specificity. In the model mice bearing both PSMA-positive (22Rv1) and negative (PC3) tumors, the uptake of [^{68}Ga]PSMA-11 in the 22Rv1 tumor (2.7 ± 0.3%ID/g) was six-fold greater than the PC3 tumor (0.5 ± 0.1%ID/g), demonstrating that [^{68}Ga]PSMA-11 bound selectively to the PSMA-positive,

PSMA-rich tumors ($P = 0.0030$, $t(df) = 6.430(4)$). In model mice bearing only 22Rv1 tumors, the inhibition of [^{68}Ga]PSMA-11 uptake was significant before and after 2-PMPA treatment, measuring -57.8 ± 15.9%ID/g ($P = 0.0485$, $t(df) = 2.806(4)$), thereby demonstrating that [^{68}Ga]PSMA-11 bound specifically to the PSMA-positive tumors.

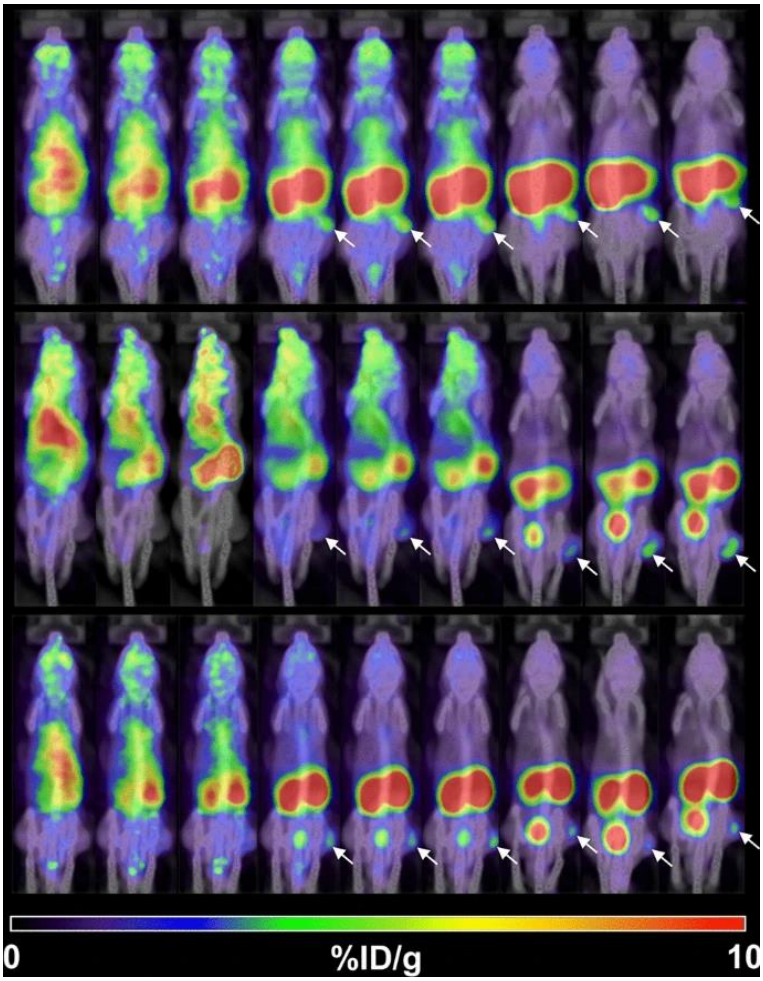

Figure 2.1 PET/CT images of the subcutaneous prostate cancer xenograft model mice ($n = 3$, each row) at various time points (from left to right in each column: 2, 5, 10, 30, 60, 90, 180, 240, 300 min *p.i.*, respectively) after the intravenous injection of [^{68}Ga]PSMA-11. The arrows indicate the PSMA-positive tumor (22Rv1). %ID/g, percent injected dose per gram of tissue).

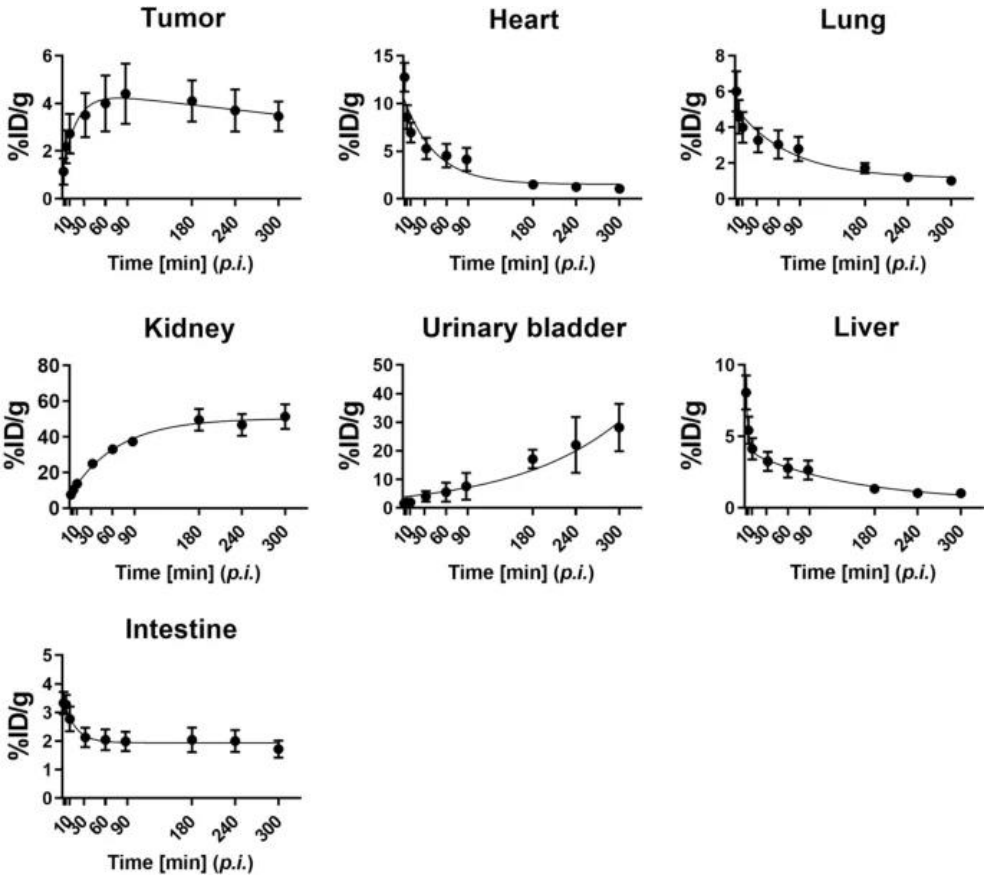

Figure 2.2 Time courses of [^{68}Ga]PSMA-11 distribution in the PSMA-positive tumor (22Rv1) and various organs. The solid lines represent the non-linear least-squares fitted optimization results for the association or dissociation model. The measurement points represent the mean ± SEM ($n = 3$).

Table 2.1 Pharmacokinetic parameters of [^{68}Ga]PSMA-11

Organ	T_{max} (min)	C_{max} (%ID/g)	AUC (%ID/g·min)	$T_{1/2}$ (min)
Tumor	118.67 ± 30.67	4.51 ± 0.69	1153.4 ± 148.7	708.2
Heart	0.58 ± 0.00	30.73 ± 4.85	906.4 ± 196.9	30.24
Lung	0.58 ± 0.00	12.76 ± 3.33	658.9 ± 137.0	51.93
Kidney	260 ± 40.00	51.97 ± 6.43	12,168.7 ± 819.2	Accumulated
Urinary bladder	260 ± 40.00	28.65 ± 7.81	4197.0 ± 1414.3	Accumulated
Liver	2.14 ± 0.31	8.64 ± 1.23	606.5 ± 102.8	100.5
Intestine	1.64 ± 0.56	4.04 ± 0.27	614.5 ± 108.0	11.6

Values are the mean ± SEM (n = 3).

Internal radiation dosimetry

The Monte Carlo simulation successfully generated the corresponding dose distribution maps for each voxelized source—i.e., the [^{68}Ga]PSMA-11 PET images (uncorrected for radiation decay) of every time-point, which represent the amount of radioactive decay at a given time-point in the simulation of the interaction between particles and materials—against the voxelized-phantom—i.e., the CT images of every time-point, which represent materials such as air, air-body interface, soft tissue, and bone that were segmented according to the threshold of the Hounsfield unit values used in the simulation—of each individual mouse (**Figure 2.3**). Because the voxel values, which indicate the temporal changes in dose (dose rate) at each time-point, in the dose maps are expressed in Gy/s, organ-specific absorbed doses are represented by dividing the integral sum of the area under the dose rate curve for each organ by the administered radioactivity (**Figure 2.4**). The calculated absorbed doses are summarized in **Table 2.2**, along with the results estimated using the MIRD-recommended organ-level method.

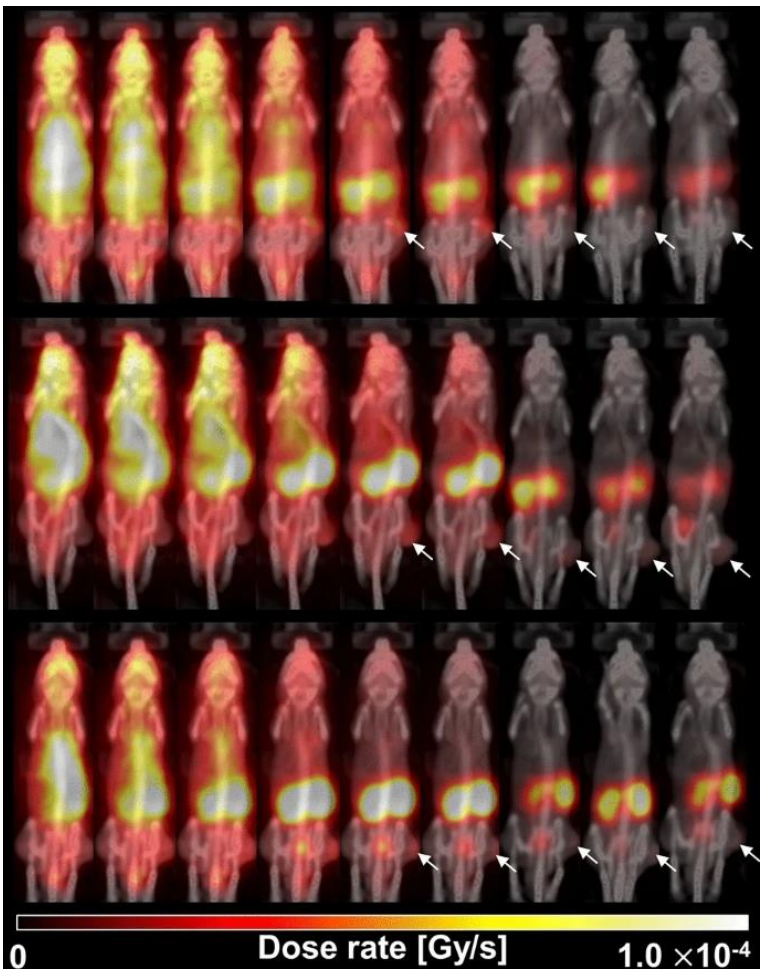

Figure 2.3 Dose map of [^{68}Ga]PSMA-11 in the subcutaneous prostate cancer xenograft model mice ($n = 3$, each row) at various time-points (from left to right in each column: 2, 5, 10, 30, 60, 90, 180, 240, 300 min *p.i.*, respectively) after the intravenous injection of [^{68}Ga]PSMA-11. The arrows indicate the PSMA-positive tumor (22Rv1).

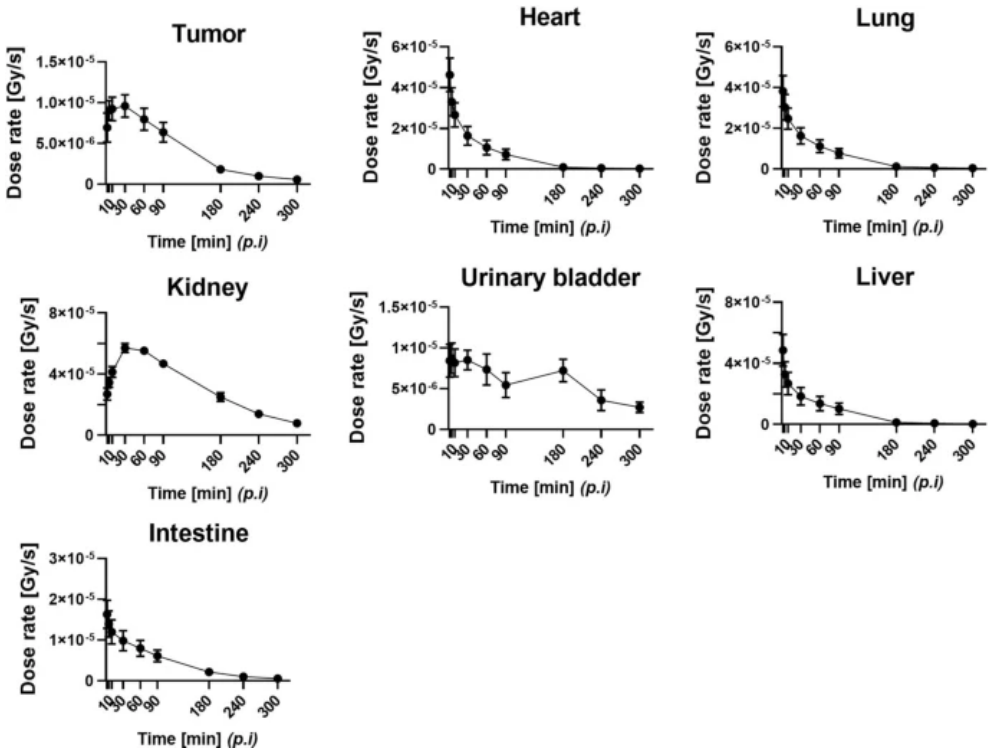

Figure 2.4 Dose rate curves of [^{68}Ga]PSMA-11 in the PSMA-positive tumor (22Rv1) and various organs. Values are the mean ± SEM ($n = 3$).

By inspecting voxel levels, it is observed that the level of [^{68}Ga]PSMA-11 accumulation corresponds to the level of the absorbed dose in each organ. The absorbed dose was the highest in the kidneys (0.209 ± 0.005 Gy/MBq), followed by the liver, urinary bladder, and lungs. The variance in the urinary bladder may be attributed to individual differences in excretion. The ability of voxel-level dosimetry in estimating the absorbed dose demonstrated a significant advantage compared to the conventional organ-level method. In the tumor, the absorbed dose estimates were 0.024 ± 0.003 Gy/MBq, whereas those were not estimated by organ-level dosimetry due to the lack of subject-specific tumor geometry in the MIRD-phantom. Because the voxel-level method considers inhomogeneous activity distribution and tissue heterogeneity throughout the entire body, the voxel-level method was expected to yield a more realistic and accurate voxel-level dose distribution in organs, such as the heart, which consist of the distinguished component.

Table 2.2 Absorbed dose received by organs of the subcutaneous prostate cancer xenograft model mice after [^{68}Ga]PSMA-11 administration.

Organ	Absorbed dose (Gy/MBq)		Difference (Organ-level – Voxel-level)	*P*-value
	Voxel-level	Organ-level		
Tumor	0.024 ± 0.003	NA	NA	NA
Heart	0.034 ± 0.009	0.055 ± 0.010	0.021 ± 0.004	0.0225
Lung	0.035 ± 0.008	0.045 ± 0.009	0.009 ± 0.001	0.4845
Kidney	0.209 ± 0.005	0.492 ± 0.059	0.283 ± 0.055	0.0088
Urinary bladder	0.038 ± 0.010	0.451 ± 0.199	0.413 ± 0.188	0.1065
Liver	0.041 ± 0.012	0.025 ± 0.002	-0.016 ± 0.010	0.2186
Intestine	0.026 ± 0.004	0.013 ± 0.000	-0.014 ± 0.003	0.0227

Values are the mean ± SEM (n = 3). NA, not applicable.

The level of [^{68}Ga]PSMA-11 accumulation corresponded to the absorbed dose in each organ. Using the voxel-level to ascertain dose absorption, the greatest absorbed dose was recorded in the kidneys, measuring 0.209 ± 0.005 Gy/MBq, compared to 0.492 ± 0.059 Gy/MBq estimated via the organ-level method. The differences in the absorbed dose of every organ demonstrated the differences in real mice compared with virtually designed or phantom mice. Statistical differences were recorded in the absorbed doses calculated via the voxel-and organ-level methods for the heart, intestine, and kidneys. The ^{68}Ga S-values for the walls of the heart and small intestine that were applied in the 25 g mouse model used in this study might also be the reason for such differences [12], as it was difficult to distinguish heart wall and between small intestine accurately during the image-based analysis. In addition, the high accumulation of [^{68}Ga]PSMA-11 without washout might be reflected in the self-absorbed dose for the kidney and, if so, would constitute the biggest difference. Moreover, without considering the time-related biodistribution, the S-values corresponding to non-labeled ^{68}Ga radioisotopes may cause discrepancies.

The effective dose of [^{68}Ga]PSMA-11 for humans using normalized residence times was converted from the mouse residence times and IDAC/Dose2.1 software according to a method proposed by Garrow et al. [54]. The predicted clinical effective dose was 0.0202 ± 0.0013 mSv/MBq, which is comparable to results reported for human subjects [63]. However, it is unrealistic to calculate the absorbed dose based on tumor-bearing animal models by conventional dosimetry because the pathophysiologic effects between human and animal models differ considerably.

2.3.2 [^{18}F]PSMA-1007

Biodistribution and pharmacokinetic

Figure 2.5 and **Figure 2.6** shows the biodistribution and clearance of [^{18}F]PSMA-1007 for PSMA-positive tumor (LNCaP)-bearing mice after intravenous injection. It illustrates rapid whole-body distribution immediately after the injection, followed by rapid washout (at variable rates) from peripheral organs, including the liver, whereas other organs, namely the kidneys, urinary bladder, and the tumor, demonstrated accumulating uptake of [^{18}F]PSMA-1007. The pharmacokinetic parameters for the visualized organs and the tumor are summarized in **Table 2.3**. The kidneys showed the highest accumulation of [^{18}F]PSMA-1007 without exhibiting a washout phase during the study. The urinary bladder (342.31 ± 36.63%ID/g × min) was the predominant excretion route after the intravenous injection of [^{18}F]PSMA-1007 with almost four-fold greater accumulation than that in the intestine (93.35 ± 9.98%ID/g × min). The tumor exhibited a peak [^{18}F]PSMA-1007 concentration of 2.86 ± 0.24%ID/g at 112 min (on average) after the injection. The off-target accumulation of [^{18}F]PSMA-1007 in the salivary glands during PSMA-targeting radiopharmaceutical therapy was substantial and exhibited a greater than that in the tumor. However, the predominant hepatobiliary excretion against the urinary bladder was only observed in human species, whereas in a preclinical environment using mice or rats, a renal dominant clearance has been described [34]. [^{18}F]PSMA-1007 continuously accumulated in the kidney and the urinary bladder, whereas its uptake was lower in the liver and the intestine. The difference is attributable to the biological differences between human and animal subjects in particular; the specific activity of [^{18}F]PSMA-1007 varied unavoidably across studies.

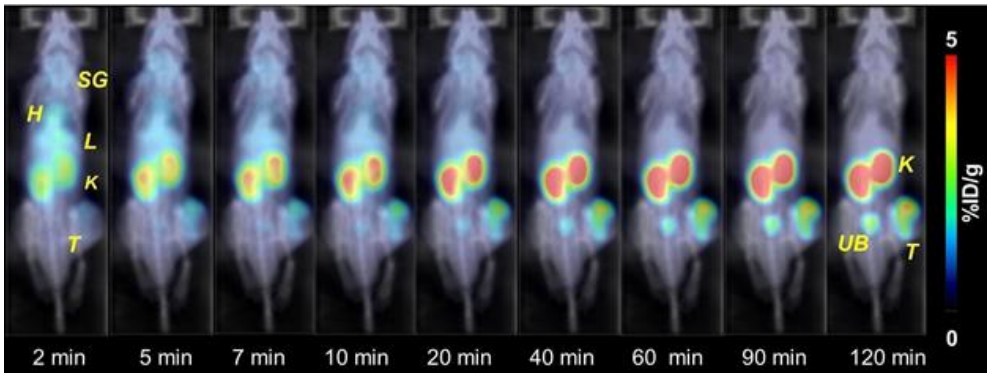

Figure 2.5 Serial PET/CT images of a subcutaneous prostate cancer xenograft mouse model after injection with [^{18}F]PSMA-1007. PET/CT, positron emission tomography/computed tomography; %ID/g, percent injected dose per gram of tissue; H, heart; K, kidney; L, liver; SG, salivary glands; T, PSMA-positive tumor (LNCaP); UB, urinary bladder.

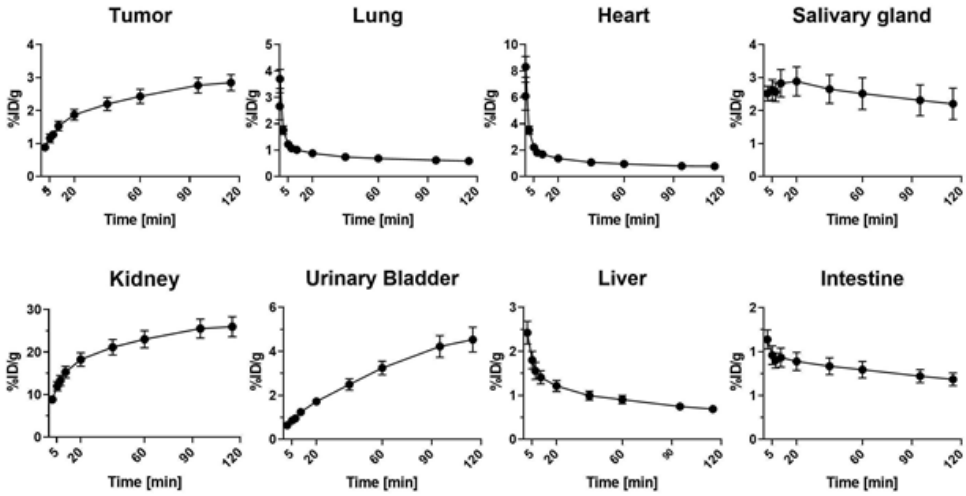

Figure 2.6 Percentage of injected dose per gram (%ID/g) of [^{18}F]PSMA-1007 over time. The data points represent the mean and the error bars represent the standard error of the SEM (n = 8).

Table 2.3 Pharmacokinetic parameters of [^{18}F]PSMA-1007

Organ	T_{max} (min)	C_{max} (%ID/g)	AUC (%ID/g·min)	$T_{1/2}$ (min)
Tumor	112.5 ± 1.64	2.86 ± 0.24	260.98 ± 22.99	Accumulated
Salivary gland	9.25 ± 3.36	3.25 ± 0.39	286.28 ± 48.67	238.99 ± 82.52
Heart	0.21 ± 0.03	8.88 ± 0.82	132.12 ± 9.54	0.79 ± 0.12
Lung	0.21 ± 0.03	3.94 ± 0.37	88.42 ± 7.97	0.39 ± 0.15
Kidney	108.75 ± 2.63	26.10 ± 2.32	2483.88 ± 219.37	Accumulated
Liver	0.38 ± 0.05	4.18 ± 0.47	116.15 ± 12.30	0.44 ± 0.21
Intestine	1.13 ± 0.25	1.47 ± 0.14	93.35 ± 9.98	222.73 ± 39.93
Urinary bladder	110.63 ± 4.38	4.54 ± 0.57	342.31 ± 36.63	Accumulated

Values are the mean ± SEM (n = 8).

Repeatability and Specificity

The mean TAC of [^{18}F]PSMA-1007 (SUV) in the tumor of the same animal overlapped completely between scans performed over two consecutive days. The respective fitted TACs in C_{NS} and Cs and corresponding parameters (K_1–k_3 estimates and the net influx rate constant *Ki*) are summarized in **Figure 2.7A** and **Table 2.4**, respectively. There is no significant difference in kinetic parameters between scans ($P > 0.05$). Based on the AUC (in the unit of SUV × min), the wCV was 7.57%, the RC was 20.98%, and the ICC was 0.950 (95% confidence interval [CI] for ICC: 0.775, 0.99, $P < 0.001$). For SUV after 1 h, the wCV was 7.75%, the RC was 21.47%, and the ICC was 0.949 (95% CI for ICC: 0.775, 0.99, $P < 0.001$).

Differences in SUV between the baseline and inhibition groups induced by 2-PMPA treatment (50 mg/kg) demonstrated the specific binding of [^{18}F]PSMA-1007 in the PSMA-positive tumor (LNCaP). In both the baseline and inhibition groups, the mean SUV in the tumor increased over time, with marked differences in the slope between groups; however, the TACs in the 2T3k showed a good fit in both groups. The fitted TACs for C_{NS} and Cs and corresponding parameters of the modeling are summarized in **Figure 2.7B** and **Table 2.4**. The 2-PMPA treatment altered k_2 (efflux to the blood) and k_3 (influx to the specific binding tissue), but not K_1 (influx to the non-specific binding tissue) and led to a 32% decrease in K_i (the net influx rate constant to the specific binding tissue) of [^{18}F]PSMA-1007 in the tumor ($P = 0.0203$).

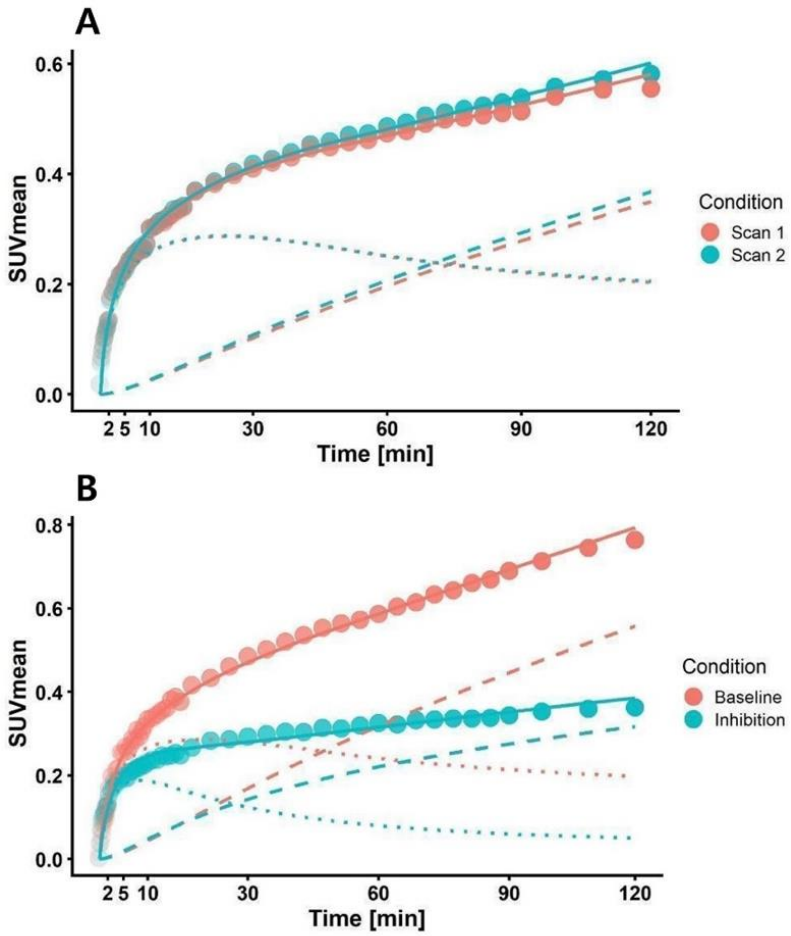

Figure 2.7 (A) Time-activity curves (TACs) of [^{18}F]PSMA-1007 in the irreversible two-tissue compartment model (2TCM). All tumors in the test and retest groups were evaluated (n = 8 in each group). (B) TACs of [^{18}F]PSMA-1007 in the irreversible 2TCM of the baseline and PSMA-inhibition groups. The data points represent the mean standard uptake value (SUV) of tumors determined by PET images. The solid lines represent the SUV estimates of a tissue compartment (C_T) using parametric parameters, dashed lines represent the SUV of a specific binding compartment (Cs), and dotted lines represent the SUV of a non-specific binding compartment (C_{NS}).

Table 2.4 Estimated kinetic parameters (K_1–k_3) and the net influx rate constant (K_i) of [^{18}F]PSMA-1007 for the irreversible two-tissue compartment model in the repeatability and specificity studies

Study	Group	K_1 (1/min)	k_2 (1/min)	k_3 (1/min)	Influx-K_i (1/min)
Repeatability	Scan 1	0.057 ± 0.015	0.036 ± 0.022	0.013 ± 0.003	0.016 ± 0.004
	Scan 2	0.057 ± 0.016	0.033 ± 0.015	0.014 ± 0.005	0.017 ± 0.005
	P-value	0.9573	0.7894	0.6439	0.7035
Specificity	Baseline	0.062 ± 0.020	0.032 ± 0.010	0.022 ± 0.002	0.026 ± 0.006
	Inhibition	0.066 ± 0.013	0.089 ± 0.012	0.029 ± 0.005	0.018 ± 0.005
	P-value	0.7581	0.0127*	0.3514	0.0203*

The twice PET/CT scans (Scan 1 and Scan 2) in the same eight mice were compared in a repeatability group. The inhibition group was treated with 2-PMPA (50 mg/kg, $n = 5$ in each group). Data were generated using an irreversible two-tissue compartment model. All data are presented as mean ± SEM. *$P < 0.05$

Internal radiation dosimetry

The voxel-level dosimetry method demonstrated a significant advantage in estimating the absorbed dose over the organ-level method. In the tumor and the salivary glands, the absorbed dose estimates were 78.25 ± 10.08 mGy/MBq and 35.94 ± 6.42 mGy/MBq, respectively, whereas these values could not be estimated by organ-level dosimetry due to the lack of subject-specific tumor geometry in the MIRD-phantom. **Figure 2.8** and **Figure 2.9** display the E_{dep} maps and dose rate curves over time obtained from the Monte Carlo simulations, respectively.

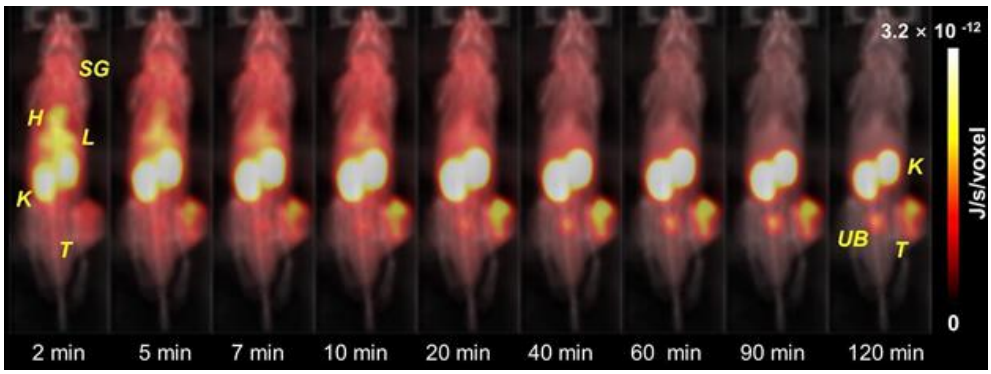

Figure 2.8 E_{dep} maps of [^{18}F]PSMA-1007 in tumor lesions and various organs of xenograft model mouse after injection with [^{18}F]PSMA-1007. H, heart; K, kidney; L, liver; SG, salivary glands; T, PSMA-positive tumor (LNCaP); UB, urinary bladder.

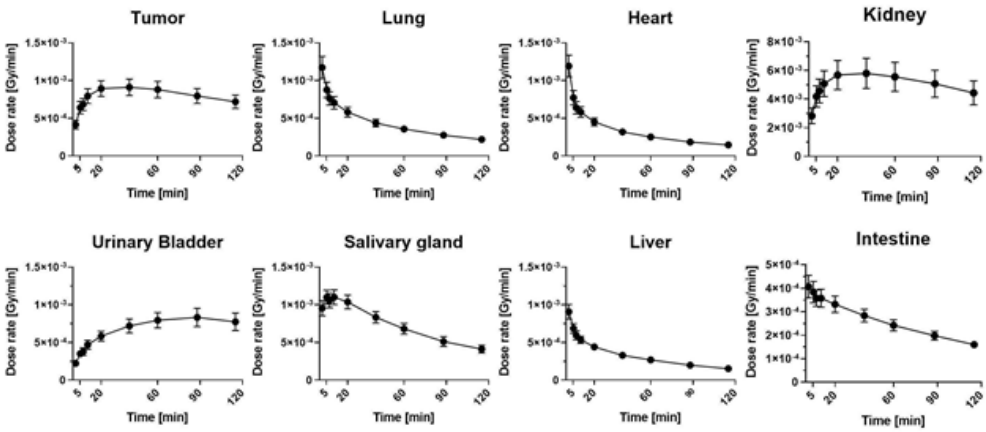

Figure 2.9 Dose rate curves of [^{18}F]PSMA-1007 in tumor lesions and various organs of xenograft model mice. The data points represent the mean, and the error bars represent the SEM (n = 8).

In **Table 2.5**, the kidneys showed the highest absorbed dose (organ-level: 378.81 ± 43.97 mGy/MBq; voxel-level: 441.50 ± 59.10 mGy/MBq), whereas the highest absorbed dose was observed in the urinary bladder (441.00 ± 83.18 mGy/MBq) for the organ-level method. The absorbed dose in the other organs, excluding the kidneys, urinary bladder, salivary glands, and the tumor, ranged from 11 to 16 mGy/MBq and from 4 to 14 mGy/MBq, for voxel- and organ-level methods, respectively. Furthermore, the largest difference between the methods was observed in the urinary bladder and kidney, possibly due to the underlying principles of estimation.

Table 2.5 Absorbed dose received by organs of the subcutaneous prostate cancer xenograft model mice after [^{18}F]PSMA-1007 administration.

Organ	Voxel-level (mGy/MBq)	Organ-level (mGy/MBq)	Difference (Organ-level – Voxel-level) (mGy/MBq)
Tumor	78.25 ± 10.08	NA	NA
Salivary glands	35.93 ± 6.42	NA	NA
Heart	10.90 ± 0.82	13.88 ± 1.12	2.98 ± 0.64
Lungs	15.83 ± 1.04	12.32 ± 1.18	–3.50 ± 0.55
Kidneys	441.50 ± 59.10	378.81 ± 43.97	–62.70 ± 38.75
Liver	11.76 ± 0.82	4.25 ± 0.43	–7.51 ± 0.81
Intestine	13.19 ± 0.76	3.66 ± 0.33	–1.84 ± 0.76
Urinary bladder	54.16 ± 13.37	441.00 ± 83.18	364.35 ± 72.57

All data are presented as mean ± SEM (n = 8). NA, not applicable.

The absorbed dose in the tumors and salivary glands at the organ-level by using an alternative approach was estimated, which involved using the IDAC Spheres embedded in the IDAC-Dose 2.1 software sub-module for adult reference voxel phantom [47]. The absorbed dose calculated by the dosimetry software using real mouse-specific organ volume and residence time was 42.47 ± 12.60 mGy/MBq in the tumors and 212.98 ± 44.57 mGy/MBq in the salivary glands. Using the voxel-level method, the absorbed doses in the tumors and salivary glands were estimated to be 78.25 ± 10.08 mGy/MBq and 35.93 ± 6.42 mGy/MBq, respectively. The effective dose of 1.12E-02 ± 1.39E-04 mSv/MBq was predicted based on ICRP adult reference voxel phantoms and was less than that predicted by a previous clinical study [31,47].

2.4 Discussion

In this study, image-based internal radiation dosimetry methods at organ-/ voxel-level were developed and established by using two promising prostate cancer diagnostic radiopharmaceuticals-[^{68}Ga]PSMA-11 and [^{18}F]PSMA-1007. In response to the rapid growth in the demand for clinically robust estimations of the dose-response relationships for therapeutic radiopharmaceuticals, PET and/or SPECT are being increasingly deployed to characterize the biodistribution, pharmacokinetics, and internal radiation dosimetry of novel companion diagnostic or theranostic radiopharmaceuticals in disease/target-specific xenograft animal models. Furthermore, to provide a basis for clinical dose selection, dose-response relationships, and safety in terms of internal radiation dosimetry and to endorse further investigation for use in personalized medicine and TRT in cancer patients.

[^{68}Ga]PSMA-11 and [^{18}F]PSMA-1007 in the xenograft model mice were satisfy several criteria to be considered for clinical cancer diagnosis, such as rapid washout from the background but high and lasting uptake in the target, thereby guaranteeing significant contrast for clear visualization and accurate quantification. The intravenously administered radiopharmaceuticals promptly exhibited whole-body distribution followed by rapid washout (at variable rates) for peripheral organs. The uptake in the tumors also showed a significant contrast for clear visualization and accurate quantification. The quantitative performance of two diagnostic radiopharmaceuticals was investigated by performing selectivity and specificity for [^{68}Ga]PSMA-11 and selectivity and repeatability for [^{18}F]PSMA-1007.

The MIRD-recommended organ-level dose calculation was applied and the GATE Monte Carlo simulation was selected to compute the voxel-level absorbed dose in

xenograft model mice. Although the use of generalized formalism (organ-level) is time- or cost-effective, direct Monte Carlo simulation addresses tissue heterogeneity and subject-specific variation in the activity distribution of real animal models using PET/CT imaging.

Various studies have attempted to minimize the dose-limiting side-effect in the off-target organs and tissues to optimize TRT [64,65]. Although the salivary gland is a dose-limiting organ of PSMA-TRT, it is not possible to estimate the actual absorbed dose using the MIRD schema at the organ-level. As the S-values of several organs and abnormal organs in normal mice were not determined in the general MOBY mouse phantom model, an alternative method was applied to the organ-level absorbed dose. However, this alternative method has several drawbacks. The IDAC Spheres sub-module assumes that the tumor and salivary glands are a virtual uniform sphere, and the distribution of radiopharmaceuticals is homogeneous regardless of the tumor shape, location, and tissue density [47]. Additionally, it is not applicable in mice given that mouse and human anatomical features and energy transport in these organs were determined the same and the IDAC-Dose 2.1 has been developed specifically for estimating the absorbed dose in humans. Furthermore, lower absorbed doses tend to be erroneously estimated with larger organ volumes, as the tissue density is fixed. This suggests that voxel-level dosimetry could yield more realistic and accurate results, particularly in abnormal organs.

However, no correlation between the tumor volume and voxel-level absorbed dose was observed, unlike the sphere model. With a dedicated tool, it is expected to yield a more realistic and accurate voxel-level dose distribution in organs because it considers inhomogeneous activity distribution and tissue heterogeneity throughout

the entire body [2]. For example, the heart-absorbed dose using dose rate (Gy/s) in all voxels of the heart volumes of interest (VOIs) is estimated in voxel-level dosimetry without distinguishing blood and the wall of the heart. Thus heart-absorbed dose may be expected to overcome the issue of the conventional organ-level (or phantom-based) method.

Furthermore, the dose maps after direct Monte Carlo simulation are produced from the voxelized source and voxelized phantom, which were resampled from subject-specific PET/CT images and represented the inputs. From this point of view, it reminds us of the value of evaluating personalized voxel-level dosimetry in various cases, such as localization, metastatic tumors, heterogeneous activity distribution, and organ geometry.

The image-based dosimetry method was applied at organ-/voxel-level and absorbed dose estimates from diagnostic radiopharmaceuticals–[^{68}Ga]PSMA-11 and [^{18}F]PSMA-1007 PET/CT– in a subcutaneous prostate cancer xenograft mouse model support clinical therapeutic strategies that use paired therapeutic radiopharmaceuticals (such as [^{177}Lu]PSMA-617) [34,66]. Especially, the quantitative radiation dose estimates for target lesions could be fundamental evidence for use of surrogates (e.g., companion diagnostic radiopharmaceuticals, theranostic pair) while minimizing radiation-induced toxicity to off-target tissues. Further research is required to investigate more reliable new methods than organ/whole body weight normalization for translating human absorbed dose from the preclinical study and gather sufficient evidence about determining the human effective dose of [^{177}Lu]PSMA-617 directly from preclinical xenograft model mice after administrating surrogates.

2.5 Summary

In this study, a preclinical image-based internal radiation dosimetry was successfully established in subcutaneous xenograft model mice after injecting promising diagnostic radiopharmaceuticals, and these applications showed great promise for use in patient-specific dosimetry. Preclinical dosimetry can provide a starting point for the radiobiological interpretation and modeling of the dose distribution for response assessment during cancer therapy. The absorbed dose estimates of promising diagnostic radiopharmaceuticals for the detection of prostate cancers with high specificity, [^{68}Ga]PSMA-11 and [^{18}F]PSMA-1007, were comparable to results reported for human subjects [63]. Particularly, dosimetry at the voxel-level was used to accurately determine the absorbed dose not only in major organs but also in abnormal tumors and dose-limiting critical organs, such as the salivary glands and kidneys. As the aim of TRT is to minimize the dose-limiting side-effect in the off-target organs and tissues to optimize [64,65], the tumor and critical organs' absorbed dose per respective prostate cancer xenograft model mice using direct Monte Carlo simulation may be meaningful preliminary data.

Furthermore, the voxel-level dosimetry paradigm of companion radiopharmaceuticals sharing a similar motif of therapeutics can apply to estimate quantitative radiation doses for alpha-/beta-particle emitter labeled therapeutics instead of using non-/less quantitative molecular images and implement the personalized TRT and precision medicine. The approach of voxel-based dosimetry of companion diagnostics proposed in the present study could be used for assessing the three-dimensional distribution of the absorbed dose for alpha- and/or beta-particle emitter-labeled therapeutics, for which estimating the radiation doses

quantitatively is difficult via imaging. For example, ^{225}Ac-DOTATATE coupled with ^{68}Ga-DOTANOC in targeted alpha therapy of neuroendocrine tumor [67], ^{225}Ac-labeled hNd2 (NMT25) coupled with ^{89}Zr-labeled hNd2 (NMK89) for therapy of pancreatic cancer [68], and ^{225}Ac-DOTA-hTAB004 coupled with ^{111}In-DOTA-hTAB004 for therapy of breast cancer [69].

Chapter 3. The investigation of the theranostic surrogacy of companion diagnostic radiopharmaceutical for radionuclide therapy

3.1 Background

Differentiated thyroid cancer (DTC) is the most common endocrine malignancy arising from follicular cells in the thyroid. DTC treatment includes radioiodine therapy, which involves the systemic administration of [^{131}I]NaI for the irradiating thyroid remnants. A sodium iodide symporter (NIS, encoded by the SLC5A5 gene) mediates radioidine therapy for DTC to incorporate radioiodine into cancer cells, which is expressed in the basolateral plasma membrane of thyroid follicular cells and mediates the active transport of radioiodine from the bloodstream into the follicular cells [70,71].

The radioiodine dose for treating DTC is performed by either administering an empiric fixed dose (3.7–7.4 GBq (100 –200 mCi)) of ^{131}I (Dorn et al. 2003) or using dosimetry-guided techniques [72], from which the most optimal dose has been discussed and investigated. Several regulatory organizations have recommended the guidelines for ^{131}I therapy [73,74], and the empiric fixed dose was chosen based on physicians' experience and patient's condition (e.g., surgical adjuvant procedure, recurrent lesions, tumor histotypes, and intolerance to surgery or therapy). Previous studies supported the high efficacy of the dosimetric activity of ^{131}I for the treatment of high-risk patients with DTC [75], and dosimetry-guided ^{131}I treatment allows the administration of a maximum possible dose to achieve the maximum therapeutic

benefit with a minimum dose to critical organs, such as bone marrow and hematologic toxicity [76,77].

[^{131}I]NaI planar scans at multiple time points combined with blood sampling have generally been used for dosimetry [78,79]. Although ^{131}I simultaneously emits two types of radiation–β^- for treatment and γ for diagnosis, just less than 10% of ^{131}I decay products which are suitable for imaging. Moreover, poor imaging makes it difficult to quantify heterogeneous inter-/intralesional uptake and inaccurate lesion masses, affecting the dose–response relationship. Furthermore, a high-energy (HE) collimators applied for ^{131}I imaging are rarely prepared for an animal-dedicated single photon emission computed tomography(SPECT)/computed tomography(CT) systems. Lee et al. reported I-131 trastuzumab imaging and radiation dosimetry using a pinhole collimator attached to a conventional gamma camera [80].

In preclinical and clinical studies, imaging radionuclide-labeled surrogates can be used to overcome such limitations and assess therapeutic absorbed doses. An immediate challenge is the validation of extrapolation between two radionuclides with different physical half-lives. Few reports have compared diagnostic and therapeutic radiopharmaceuticals; instead, it is assumed that theranostic pairs have similar biodistributions and pharmacokinetics [81–83].

^{124}I, an imaging radioiodine, was used for positron emission tomography (PET) to show the facility of whole-body and lesional dosimetry in previous studies [84,85]. However, ^{124}I is a cyclotron produced and has a rather complex decay scheme. It emits over half of γ rays, which have an energy of 603 keV (11%, E_{max} = 1.7 MeV), and the energies of the $\beta+$ are high, associated with a long-range [86,87]. Hence, the surrogacy of another useful theranostic pair–^{123}I (83.3%, E_{γ}= 159 keV), was

investigated and established: ^{123}I SPECT image-based dosimetry method for DTC treatment.

Although pretherapeutic dose determination for a specific patient may be ideal, a survey identified that some facilities do not perform dosimetry for DTC treatment due to the demanding work for the staff (38%, 23/61) and inadequate reports over empirically fixed activities (43%, 26/61) [88]. As interest in TRT and personalized medicine has gained significant attention during the last decade, simplified approaches, including single-time-point (STP) dosimetry, have been developed to reduce similar challenging dosimetric processes, assuming that the radiopharmaceuticals showed a mono-exponential decay behavior for clearance in a region of interest (ROI) with an effective half-life (T_{eff}) [21–23]. Previous ^{177}Lu-PRRT studies determined that one or two measurements would be sufficient to perform renal and tumor dosimetry without fully acquired images [22,89–91], and Ardenfors et al. reported that dosimetry after one day for kidneys or after 7 days for tumors resulted in satisfactory accuracy for ^{177}Lu-DOTATATE treatments.

Likewise, alternative dosimetry methods for determining the activities of ^{131}I in patients with DTC have also been proposed to simplify blood sampling and the full whole-body measurements. Although several simplified approaches for patients with DTC helped calculate tolerated activity in the blood or bone marrow, the radiation absorbed dose to a tumor was not calculated using the alternative method [92–95]. Thus, in this study, a new simplified dosimetry method at the voxel level was developed, and its accuracy was discussed.

3.2 Experimental

3.2.1 Generation of human NIS-expressing thyroid (K1-NIS) cell lines

The Human papillary thyroid carcinoma cell line, K1 was obtained from ECACC (UK). K1 cells were maintained in culture medium, DMEM:Ham F12:MCDB 105 (2:1:1) supplemented with 10% heat-inactivated fetal bovine serum and 100× penicillin-streptomycin (Gibco). K1-NIS cells were maintained in a culture medium containing 1 μg/mg puromycin. K1 cells lacking endogenous NIS were modified to express NIS, named K1-NIS cells, by transduction using the SLC5A5 Tagged ORF clone lentiviral particle with monomeric green fluorescent protein (mGFP) and puromycin selection marker (OriGene, MD, USA) using a multiplicity of infection (MOI) of 5, 10, and 25, respectively.

3.2.2 In vitro analysis

The production of K1-NIS cells was performed successfully and validated using an in vitro assay before inoculation.

^{125}I uptake assay

K1 cells and K1-NIS cells were seeded onto a 24-well plate (1×10^5 cells/well) and were washed with warmed Hank's balanced salt solution (HBSS, Gibco, MA, USA). Cells were incubated for 30 min at 37°C with 500 μL warmed HBSS containing 0.5% bovine serum albumin (BSA, Sigma-Aldrich, MO, USA) and 10 mM of the sodium salt of 2-[4-(2-hydroxyethyl)-1-piperazinyl]ethanesulfonic acid (HEPES, pH 7.4), with 0.5 μCi of Na125I and 10 μM non-radioactive NaI, to yield a specific activity of 3.7 GBq/mmol. After incubation, cells were washed twice with ice-cold HBSS. The cells were detached using 200 μL of 1% sodium dodecyl sulfate (SDS). Cellular radioactive accumulation (100 μL of lysed cells) was measured using a gamma counter (Wizard 1480, PerkinElmer, MA, USA). The activity was normalized to the amount of total protein at the time of the assay using a bicinchoninic acid (BCA) protein assay (Thermo Fisher Scientific, MA, USA). All data are expressed as the mean ± standard deviation (SD) ($n = 4$ in each cell), and statistical significance was determined using an unpaired Student's *t*-test. Statistically significant was considered at P-value < 0.05.

Western blotting

Cells were lysed in a radio-immunoprecipitation assay (RIPA) buffer (ELPIS-BIOTECH, South Korea). Protein concentrations were determined using BCA

protein assay kits. Total protein (30 μg) was electrophoresed on 10% acrylamide gel and transferred to a PVDF membrane using a semi-dry iBlot2 transfer (Invitrogen, USA). Membranes were blocked using a 1×TBS-T solution containing 5% BSA for 30 minutes and incubated with the following primary antibodies overnight at 4°C: anti-mGFP (1:2,000; OriGene, MD, USA) or anti-β-actin (Millipore, USA; dilated 1:2,000). Antigen-antibody complexes were visualized with an anti-rabbit secondary antibody (1:1,000; Cell Signaling Technology, Inc., USA) and an enhanced chemiluminescence detection reagent (Thermo Fisher Scientific, USA).

Flow cytometry

K1 Cells and K1-NIS cells (5, 10, and 25 MOI) were incubated for 1 hour at 4°C. After washing with PBS containing 1% BSA twice, the intensity was determined using the FACS Calibur and CellQuest software (BD Biosciences, CA, USA) with 1×10^4 cells per sample. The cells were gated for GFP signals (Fluorochrome, FITC; Detection filter (nm), 530/30) based on the background signal from the non-transformed K1 cells. Data analysis was performed using FlowJo software (BD Biosciences, CA, USA), and the maximum fluorescence index (MFI) was compared according to the MOI in each K1-NIS cell.

3.2.3 Xenograft model mice

Six-week-old female BABL/c nude mice were obtained from Orient Bio, Inc. (South Korea). All animal experiments were approved by the Institutional Animal Care and Use Committee (IACUC) of Seoul National University Bundang Hospital (BA-2109-328-008). K1-NIS cells (5×10^5 cells) were subcutaneously injected into the

right thigh of mice with 150 μL of culture medium and Matrigel (1:1, BD Biosciences) in phosphate-buffered saline.

3.2.4 [^{123}I]NaI SPECT/CT

The animals underwent whole-body SPECT/CT scans using an animal-dedicated SPECT/CT system (NanoSPECT/CT, Mediso, Budapest, Hungary) with a 10 cm-axial and 12 cm-transaxial field of view (FOV). The SPECT spatial resolution was 1.2 mm full-width at half-maximum at the center of the FOV. A CT scan (semi-circular full trajectory, maximum field of view, 723 projections, 55 kVp, 1,000 ms, and 1:4 binning) was performed immediately before the SPECT scan. In the biodistribution and internal radiation dosimetry studies, whole-body SPECT/CT images of the xenograft mice were acquired at 30 min, 2, 4, 6, 13, 26, 39, and 64 hours after [^{123}I]NaI injection. All the animals were anesthetized with 2% isoflurane during the scan.

The SPECT images were reconstructed using the iterative three-dimensional ordered subset expectation-maximization algorithm with the following settings: 4 iterations, 6 subsets, full detector model, low regularization, spike filter on, voxel size 0.6 mm, and 400–600 keV energy window. SPECT data were corrected for decay, scatter, and attenuation during reconstruction. The reconstructed SPECT and CT images with a matrix size of 142 × 142 × 163 mm^3 and a voxel size of 0.6 × 0.6 × 0.6 mm^3 were finally prepared to be used in the analysis. The PMOD software (version 3.8, PMOD Technologies, Zurich, Switzerland) was used to process the SPECT and CT images, including activity normalization and registration.

3.2.5 [^{123}I]NaI SPECT/CT Image Analysis and Quantification

Biodistribution and Pharmacokinetics

The volumes of interest (VOIs) were drawn manually over the major organs (the tumor, thyroid, stomach, liver, intestine, kidney, urinary bladder, heart, and lung) on the SPECT and CT fused images, taking care to ensure that the VOIs did not overlap. The number of voxels within the VOIs drawn for an organ at each time point was averaged and multiplied by the voxel volume and tissue density to estimate the organ mass. Radioiodine uptake for each organ was estimated for each mouse by applying VOIs to the respective organs on the SPECT images. SPECT image-based biodistribution data obtained from the organs were plotted as a function of time to generate time-activity curves (TACs). For each organ, the measured activity (in kBq/cc) was normalized to the total injected activity to express the percentage of the injected dose per gram (%ID/g). The pharmacokinetic parameters of radioiodine in each organ were evaluated quantitatively using the TACs of the organs of interest: peak concentration (C_{max}), time to reach C_{max} (T_{max}), half-life ($T_{1/2}$), and area under the curve (AUC). The pharmacokinetic parameters and time integrated activity coefficient (TIAC) were calculated using the PK and PKNCA R packages [57,58], and a mono-exponential function was used to fit all organs in estimating $T_{1/2}$.

Extrapolated activity of [^{131}I]NaI

Although the assumptions that the pharmacokinetics and biodistribution of theranostic pairs are identical or similar still require further validation, sodium iodide (e.g., ^{123}I, and ^{131}I in this study) are same-element isotope pairs without chemical compounds. The radioactivity of [^{131}I]NaI was obtained from [^{123}I]NaI SPECT by

assuming that the biological half-lives of the two radionuclides are identical and can be calculated by the physical half-life of ^{123}I and ^{131}I by using the formula:

$$A_T(x,y,z,t) = A_I(x,y,z,t)\ e^{\frac{tln2}{T_{\frac{1}{2}}I}}\ e^{\frac{-tln2}{T_{\frac{1}{2}}T}}$$

Where $A_T(x,y,z,t)$: ^{131}I activity at positions x, y, and z at time *t*; $A_I(x,y,z,t)$: ^{123}I activity at positions x, y, and z at time *t*; The physical half-life of ^{123}I and ^{131}I is 13.2 h and 8.02 days, respectively [85]. Extrapolated [^{131}I]NaI radioactivity data were used for both organ- and voxel-level internal radiation dosimetry. For example, the time-integrated activity coefficients (TIAC in units of MBq×h/MBq) were obtained using a non-decay corrected TAC (%ID) of [^{131}I]NaI, and the virtual [^{131}I]NaI activity images (i.e., rescaled from [^{123}I]NaI SPECT) were generated as the corresponding dose distribution maps for each voxelized source.

Internal radiation dosimetry of [^{131}I]NaI

The analysis was performed as described in previous Chapter 2. Briefly, both organ- and voxel-level dosimetry methods were used. Each method is based on the Medical Internal Radiation Dose (MIRD) schema, which uses a generalized formalism to estimate the absorbed dose. The S-values of the ^{131}I radioisotope for the source-target organ pairs were obtained from the published database [44], and the Monte Carlo approach (applied in a dedicated software called GATE, version 9.0) was used to simulate the complete events of the radioactivity decay process, respectively [37]. In addition, it was used to estimate the absorbed dose in the major organs (including tumors) but was not estimated by organ-level dosimetry because of the lack of subject-specific geometry in the MIRD-phantom, and voxel-level absorbed dose

estimation was normalized to the activity of the injected [^{123}I]NaI for each mouse.

The simplified voxel-level absorbed dose for the tumor in the xenograft model mice

Since the absorbed dose calculation is the sum of the dose rate curves, a simplified approach to voxel-level dosimetry also begins with estimating the dose rate curves. The suggested methodology assumes that the dose rate curves follow a mono-exponential behavior with each half-life ($\lambda_1 - \lambda_3$). The three methods (M1-M3) were used to obtain the tumor absorbed dose (AD_{Mx}).

$$(AD_{Mx}) = AD_{0-T_{SC,1}} + \int_{T_{SC,1}}^{\infty} r_0 \times e^{-\lambda_x t}\, dt$$

where r_0 is the hypothetical dose rate at t = 0, which differs from the actual dose rate. The absorbed dose ($AD_{T_{SC,1}}$) before the first scan time point (t = 0 to $T_{sc,1}$) was calculated as a triangular sum. And λ_x was determined using each method (Mx), as follows:

Method 1 (M1): physical half-life of ^{131}I.

Method 2 (M2): experimental half-life of two scan time points ($T_{sc,1}$, $T_{sc,2}$); subject-specific half-life of two scan time points.

Method 3 (M3): the group mean half-life of dose rate curves up to 64 hours.

The dose rate curves were extrapolated with the half-life of each method, and the absorbed doses were calculated as an integral sum. Finally, the dose error (DE) was evaluated from the estimated absorbed dose using M1-M3 by assuming that AD_{64h} is the actual tumor absorbed dose up to 64 hours as follows [23]:

$$\text{DE } [\%] = \left(\frac{AD_{Mx}}{AD_{64h}} - 1\right) \times 100\%$$

3.3 Results and Discussion

3.3.1 In vitro analysis of NIS expression in K1-NIS cells

^{125}I uptake assay

^{125}I uptake normalized to the amount of total protein in K1 and K1-NIS cells is presented in **Figure 3.1A** and **Table 3.1**. ^{125}I uptake normalized to the amount of total protein by K1-NIS cells was 49.3 times higher than uptake by K1 cells. In addition, K1-NIS cells showed a significantly higher ^{125}I uptake ($P < 0.0001$, $t(df) = 10.31(6)$).

Table 3.1 ^{125}I uptake normalized to the amount of total protein by K1 and K1-NIS cells.

Cell	^{125}I uptake for cell amount (pmol/mg protein)	^{125}I uptake for counter per minutes (cpm/mg protein)
K1	387.9 ± 155.4	1529.8 ± 612.7
K1-NIS	19127.9 ± 3632.4	7546.5 ± 9319.1

Values are the mean ± standard deviation (SD) ($n = 4$).

Western blotting

An antibody recognizing GFP expression of the NIS protein was used, and β-actin was used as a loading control. **Figure 3.1B** shows that the NIS protein on K1 cells was successfully transferred.

Flow cytometry

The GFP expression in K1-NIS cells (5, 10, and 25 MOI) was evaluated by flow cytometry, and the MFI was compared to that of K1 cells. (**Figure 3.1C, Table 3.2**). All K1-NIS cells expressed substantially high green fluorescence, and the MFIs of K1-NIS cells were at least 106 times higher than that of K1 cells.

Table 3.2 Maximum Fluorescence Index (MFI) from flow cytometry

Cell line	MFI
K1 cell	13.7
K1-NIS cell (5 MOI)	1460.7
K1-NIS cell (10 MOI)	1279.7
K1-NIS cell (25 MOI)	2850.7

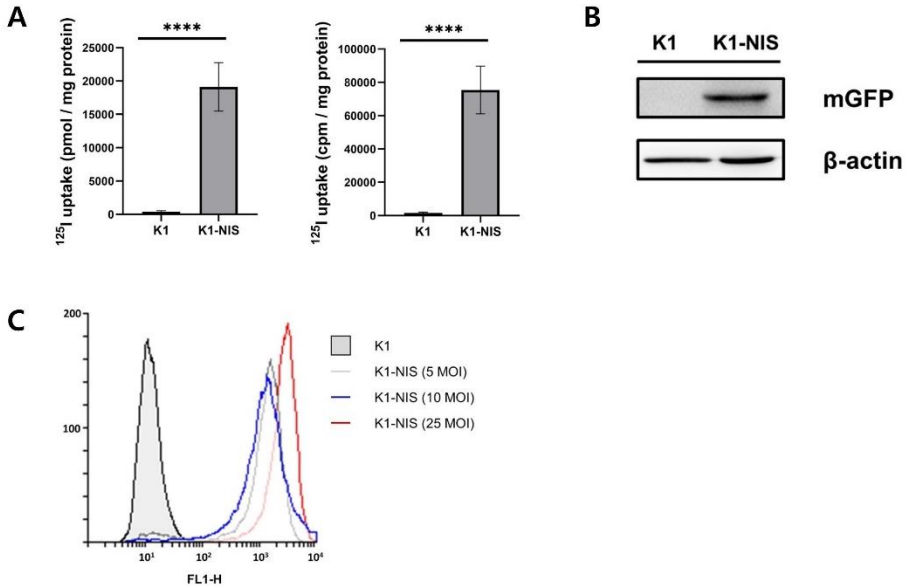

Figure 3.1 In vitro analysis of NIS expression in K1-NIS cells. (A) ^{125}I uptake assay of retrovirus-mediated NIS-transfected K1-NIS cells. All values are presented as the mean ± SD (n = 4). (B) Western blotting analysis of the mGFP expression in K1-NIS cells. (C) Analysis of GFP expression on K1-NIS cells by flow cytometry.

3.3.2 [^{123}I]NaI biodistribution and pharmacokinetics

[^{123}I]SPECT images in DTC model mice were used to illustrate the biodistribution of radioiodine and internal radiation dosimetry for tumors (**Figure 3.2**). The figure illustrates rapid whole-body distribution immediately after injection and rapid washout at variable rates. The time course of decay-corrected radioiodine for the disease model after injection is shown in **Figure 3.3**, and pharmacokinetic parameters are presented in **Table 3.3**. Since iodine is actively transported into the thyroid follicular cells via the sodium/iodide symporter (NIS), both tumors and the thyroid, which express high levels of NIS, showed substantial uptake of [^{123}I]NaI. As NIS also functions in extrathyroidal tissues [96], the pharmacokinetic characteristics of the stomach showed specifically the 34.80%ID/g peak concentration (C_{max}) 2.28 hours after administration (T_{max}), and the urinary bladder was the predominant excretion route of the intravenous injection.

To obtain reliable information for injected radiopharmaceuticals, radioactivity measurements are required several times during a time corresponding to approximately 3–5 times the effective half-life of drugs. All scan time points were determined to correspond to multiple times the physical half-life of ^{123}I (13.2 hours), and all scans were acquired for up to 64 hours. As the last scan time point was more than four-fold greater than the physical half-life of ^{123}I, [^{123}I]NaI SPECT sufficiently characterized the biodistribution, pharmacokinetics, and internal radiation dosimetry of the theranostic radiopharmaceuticals ^{131}I.

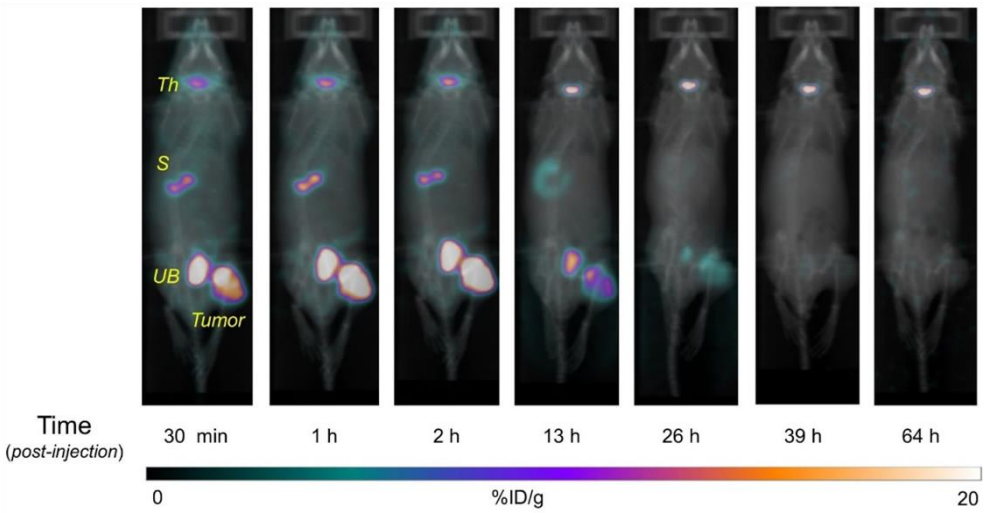

Figure 3.2 Serial SPET/CT images (corrected for radiation decay) of a DTC xenograft mouse model after [^{123}I]NaI injection. SPECT/CT, single photon emission computed tomography/computed tomography; %ID/g, percent injected dose per gram of tissue; Th, thyroid; S, stomach; H, heart; K, kidney; L, liver; SG, salivary glands; Tumor, human thyroid tumor expressing sodium iodine symporter (K1-NIS); UB, urinary bladder.

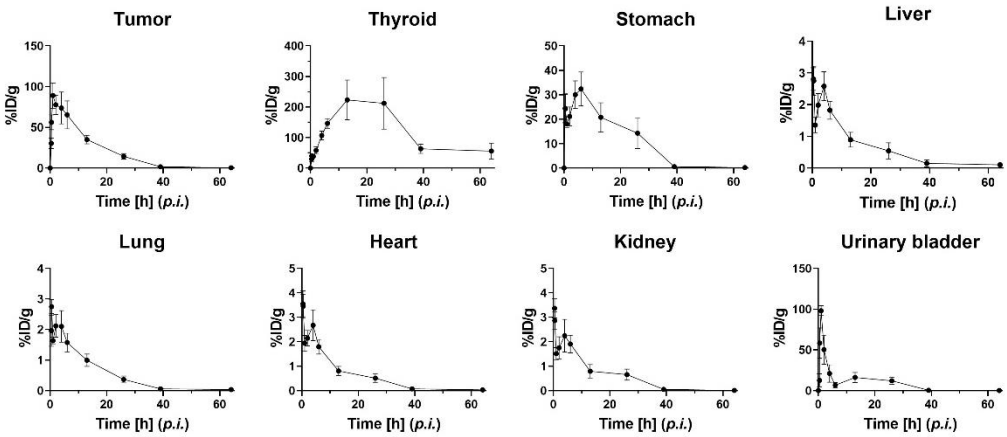

Figure 3.3 Time courses of decay corrected radioiodine distribution in the DTC xenograft mouse model and various organs. The measurement points represent the mean ± SEM ($n = 6$).

Table 3.3 Pharmacokinetic parameters of radioiodine in the DTC xenograft model mice

Organ	T_{max} (h)	C_{max} (%ID/g)	AUC (%ID/g × h)	$T_{1/2}$ (min)
Tumor	2.91 ± 0.42	96.49 ± 11.66	1252.87 ± 172.30	6.86 ± 1.10
Thyroid	21.61 ± 2.76	285.56 ± 85.80	7603.97 ± 1494.82	Accumulated
Stomach	5.28 ± 2.42	34.80 ± 8.75	654.69 ± 225.64	6.11 ± 1.21
Liver	1.29 ± 0.57	2.99 ± 0.57	34.94 ± 10.72	7.24 ± 1.26
Lung	3.03 ± 1.99	3.38 ± 0.50	33.83 ± 5.64	6.06 ± 1.91
Heart	1.03 ± 0.57	3.61 ± 0.58	36.35 ± 7.87	11.62 ± 4.57
Kidney	0.68 ± 0.26	3.18 ± 0.56	32.35 ± 8.41	8.40 ± 1.33
Urinary bladder	7.51 ± 4.14	69.50 ± 14.41	604.27 ± 98.45	6.08 ± 1.10

Values are presented as the mean ± SEM (n = 6).

3.3.3 Internal radiation dosimetry

To assess the absorbed dose by applying the published S-values of ^{131}I for the 28 g MOBY phantom mouse, the calculated TIAs from **Figure 3.4** were used to estimate the organ-level absorbed dose. Owing to limited data, the absorbed doses only in the lung, kidney, and thyroid were estimated to be 1.23E-02 ± 1.28E-03 Gy/MBq, 4.31E-02 ± 8.49E-03 Gy/MBq, and 1.30E+01 ± 2.96E+00 Gy/MB, respectively.

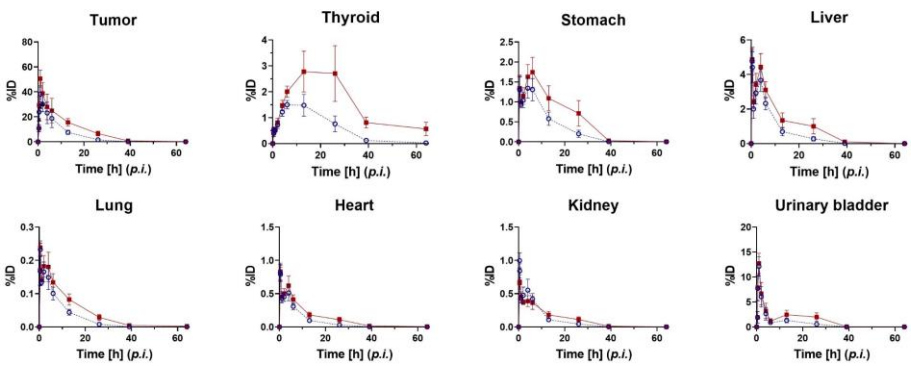

Figure 3.4 Percentage of injected dose (%ID) as a function of time obtained with [^{123}I]NaI and [^{131}I]NaI in the xenograft model mice and various organs. All dots represent non-corrected for radiation decay. The blue lines are [^{123}I]NaI distribution and the red lines are [^{131}I]NaI distribution, respectively. The measurement points represent the mean ± SEM (n = 6).

Conversely, **Figure 3.5** shows the energy deposition maps (E_{dep}) and dose distribution maps (dose map) after applying ^{131}I-ion sources to the virtual voxelized source images in the MC simulation. As surrogate radiopharmaceuticals, SPECT images were acquired until 64 hours, which is more than three times that of ^{123}I; most of the excretion phase after [^{131}I]NaI injection was observed in the organ-of-interest. The dose rate curves for each organ are shown in **Figure 3.6,** and the absorbed dose estimates are presented in **Table 3.4**. The tumor absorbed dose estimates was 0.034 ± 0.009 Gy/MBq, and the highest absorbed dose in the thyroid was 0.565 ± 0.044 Gy/MBq. As iodine accumulated in the thyroid and the excretion phase of the dose rate curve was not observed, the underestimated absorbed dose was calculated only up to 64 hours. The absorbed doses for other major organs with a full-time course of dose rate curves were comparable to the results reported for rats [97]. Although the difference in the physical half-life for diagnostic/therapeutic radionuclides is rather large, the images obtained for a long time are sufficient to estimate the absorbed doses in terms of theranostic pairs.

In this study, the biological behavior of therapeutic radiopharmaceuticals was assumed to be identical to that of imaging radiopharmaceuticals as a same-element theranostic pair. However, in the case of different-element and different-pharmaceutical theranostic pairs, various intrinsic and extrinsic factors, such as injected amounts, chemical properties, and large differences in physical half-life, may result in differences in the biodistribution and/or pharmacokinetics [19,98,99]. For example, although ^{68}Ga and ^{177}Lu are among the most popular different element pairs, [^{68}Ga]PSMA I&T is unlikely to capture the washout phase of [^{177}Lu]PSMA I&T and showed a lower concentration (%ID/g) in the tumors, kidneys, and spleen

of prostate tumor-bearing mice. Hence, before extrapolating data from imaging radiopharmaceuticals' into therapeutics absorbed dose estimates, the similarity between theranostic pairs should be validated, and further studies are required to determine surrogacy [100,101].

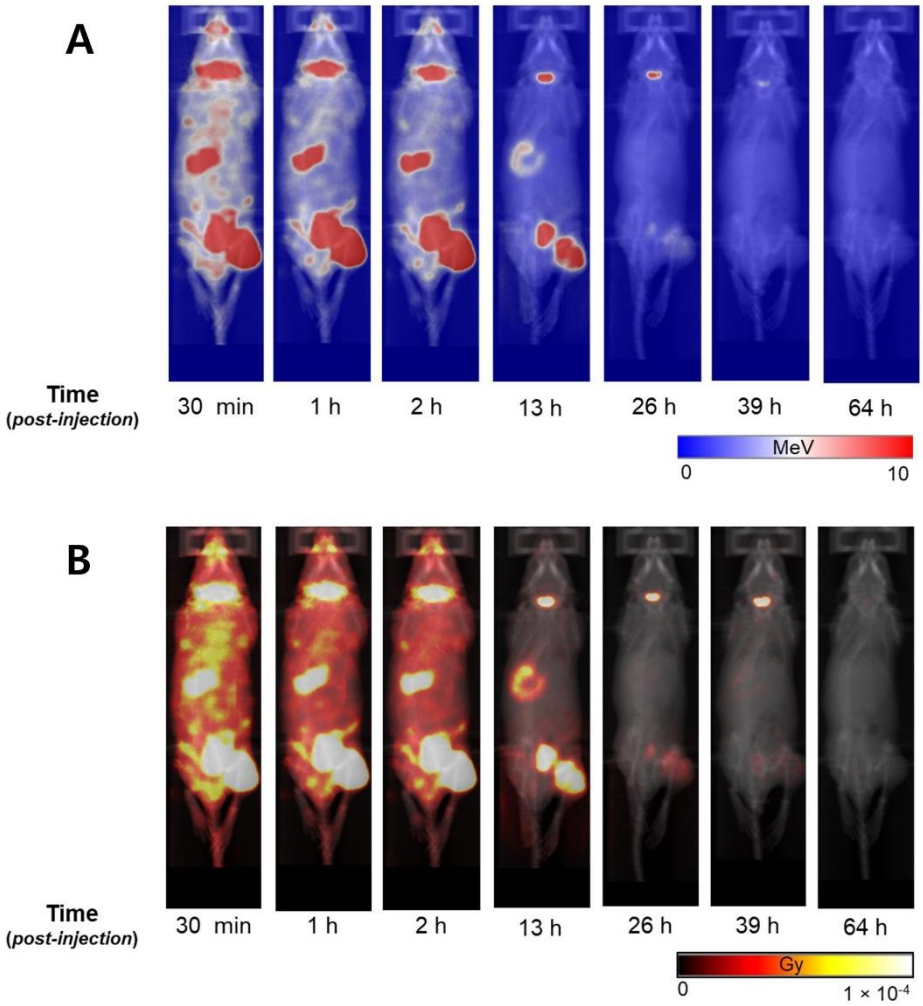

Figure 3.5 (A) E_{dep} maps and (B) Dose maps for [^{131}I]NaI overlaid on CT images of xenograft mice. The virtual voxelized source images were produced from rescaled [^{123}I]NaI SPECT images and were used as input data for GATE MC simulation. E_{dep}, energy deposition; CT, computed tomography; SPECT, single photon emission computed tomography; GATE, Geant4 application for tomographic emission; MC, Monte Carlo.

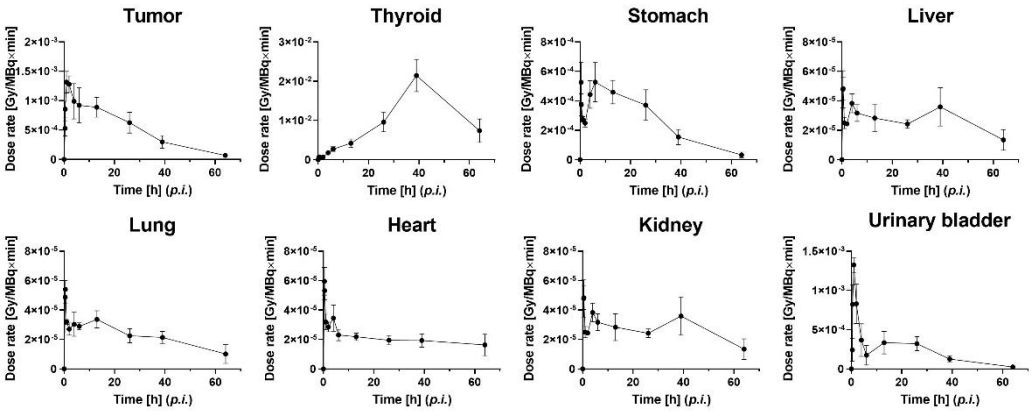

Figure 3.6 Dose rate (the mean ± SEM, n = 6) as a function of time for different organs (the tumor, thyroid, stomach, liver, lung, heart, kidneys, and urinary bladder).

Table 3.4 Absorbed dose estimates per unit injected activity of ^{131}I in the xenograft model mice.

Organ	Absorbed dose (Gy/MBq)
Tumor	0.0344 ± 0.0088
Thyroid†	0.5645 ± 0.0440
Stomach	0.0149 ± 0.0026
Liver	0.0011 ± 0.0001
Lung	0.0016 ± 0.0002
Heart	0.0018 ± 0.0007
Kidney	0.0011 ± 0.0003
Urinary bladder	0.0147 ± 0.0033

Values are presented as the mean ± SEM (n = 6).

† The absorbed dose is underestimated compared with the actual values for infinite time. As the excretion phase of the dose rate curve was not observed, the absorbed dose was assessed for up to 64 hours.

3.3.4 Simplified dosimetry in the tumors at voxel-level

Representative extrapolated dose rate curves ($T_{sc,1}$= T_{max}) are described in **Figure 3.7**. The DEs calculated from the three methods (M1-M3) are shown in **Figure 3.8**. Overall, it was observed that for the three methods, the accuracy of the absorbed dose estimates depends on the first scan time point ($T_{sc,1}$), the absorbed dose was overestimated for the earlier two scan time points. When $T_{sc,1}$ was set to time to reach peak concentration (T_{max}) with M1 and M3 methods, DE was within [-52.47%, 16.70%] and [-36.09%, 38.23%], respectively. Particularly, the most accurate absorbed dose estimates with M3 were determined when $T_{sc,1}$ and $T_{sc,2}$ were set to T_{max} and 26 hours, respectively [-22.96%, 2.21%]. However, the DEs in M2 showed the highest difference, even though they were applied with the subject-specific experimental half-lives of the dose rate curve. In other words, the absorbed dose was estimated more accurately by applying the group mean value (M3) than by applying the subject-specific value (M2). Moreover, the excretion phase of the dose rate curve was not reflected in only two scan time points data and showed high variations.

Hence, it was suggested that simplified dosimetry at the voxel level with two scan time points was possible. As the dose rate values of both two scan time points were calculated at the voxel level by considering subject-specific tissue composition and activity distribution, extrapolating dose rate curves could be predicted until the dose rate reached 0. Although T_{max} and double physical half-life of diagnostic radionuclides (=26 hours) are especially recommended for simplified voxel-level dosimetry based on this study, further research on biodistribution and

pharmacokinetic investigations for other surrogate-/therapeutic radiopharmaceuticals and applicability to other target diseases should be required.

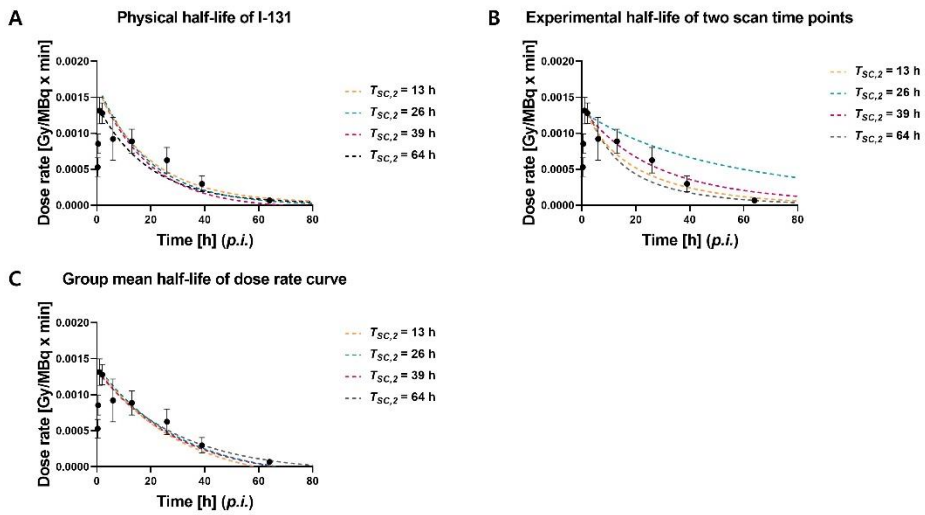

Figure 3.7 The representative dose rate curves were extrapolated using the three methods (M1-M3) as the first scan time point set at T_{max}. (A) The physical half-life of ^{131}I (M1). (B) Experimental half-life of two scan time points (M2). (C) Group mean half-life of the dose rate curve (M3). The dots represent the mean ± SEM (n = 6), and the dotted lines describe the mean of extrapolated dose rate curves as $T_{sc,2}$ is set to 13, 26, 39, and 64 hours, respectively.

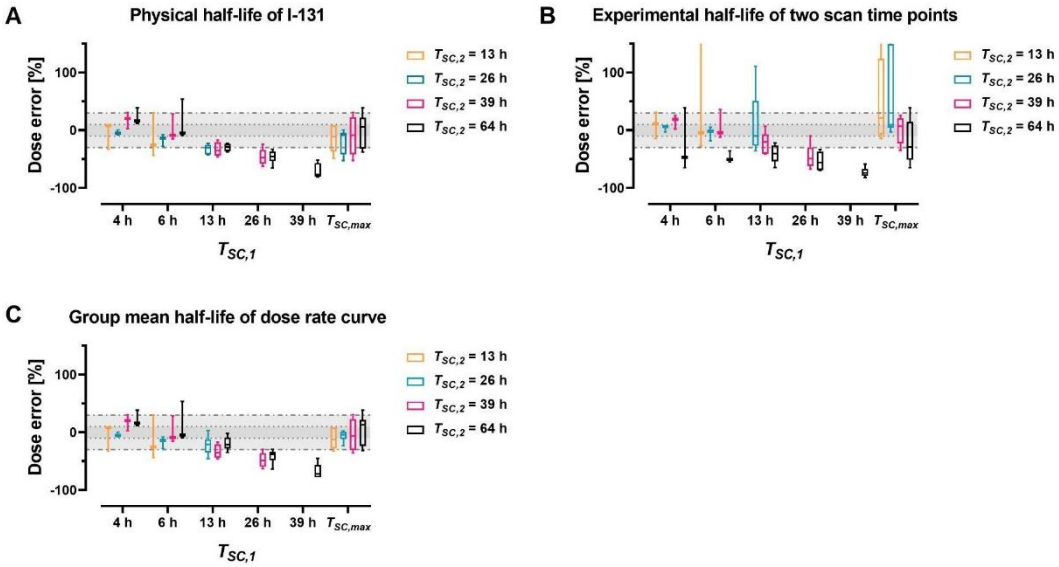

Figure 3.8 The dose error (DE) of tumor doses estimated using three methods (M1-M3). (A) The physical half-life of ^{131}I (M1). (B) The experimental half-life of two scan time points (M2). (C) The group mean half-life of the dose rate curve (M3). The dotted and dashed lines indicate ± 10% and ± 30% of DE values, respectively. ($T_{sc,1}$, first scan time point; $T_{sc,2}$, second scan time point; T_{max}, time to reach peak concentration).

In this study, a simplified approach with two scan time points was suggested for voxel-level dosimetry. Although STP dosimetry is suitable for ^{177}Lu-DOTATATE and kidney dosimetry for different radiopharmaceuticals, Hou et al., determined that at least two scans may be needed for personalized dosimetry and that these scan time points should be avoided to include the uptake phase [23]. Previous studies also demonstrated the feasibility of two-time point dosimetry calculations and showed good agreement with standard protocols [102–104]. Hence, the proposed simplified strategy could reduce the imaging protocol to two-time points for tumor-absorbed dose estimates and could be applied in precision medicine and personalized TRT.

3.4 Summary

In this study, human papillary thyroid carcinoma cell lines expressing high levels of sodium iodide symporter (NIS) protein were successfully produced by K1 cells and SLC5A5 tagged ORF clone lentiviral particles. ^{125}I uptake normalized to the amount of total protein by K1-NIS cells was 49.3 times higher than uptake by K1 cells ($P < 0.0001$, $t(df) = 10.31(6)$). Lentiviral particles, including mGFP, were used for transduction and showed expression by western blotting. The MFI of K1-NIS cells was at least 106 times higher than that of K1 cells.

After generating a total of six DTC xenograft model mice, [^{123}I]NaI SPECT/CT was obtained for 64 hours to investigate the biodistribution and pharmacokinetics of radioiodine. As theranostic pairs showed a similar distribution, ^{131}I activity was extrapolated from [^{123}I]NaI SPECT and applied as a voxelized source for producing virtual dose distribution maps of ^{131}I therapy. For the tumor, a peak concentration of 96.49 ± 11.66%ID/g occurred 2.9 hours after [^{123}I]NaI injection. Although the absorbed dose estimates for the thyroid were underestimated due to substantial accumulation, the thyroid had the highest absorbed dose (0.565 ± 0.044 Gy/MBq), and the absorbed dose for tumors was 0.034 ± 0.009 Gy/MBq.

A simplified approach for estimating tumor-absorbed dose was proposed for voxel-level dosimetry. The most accurate absorbed dose estimates with M3 were determined when $T_{sc,1}$ and $T_{sc,2}$ are set to T_{max} and 26 hours (double physical half-life of ^{123}I), respectively [-22.96%, 2.21%]. Then, simplified dosimetry at the voxel-level with two scan time points was suggested.

In this study, the perspective of simplified dosimetry was changed from the organ level to the voxel level, implying that the data utilized for simplified calculations

could be considered patient/subject-specific tissue composition and heterogeneous organ distribution. Furthermore, it demonstrated the potential for simplified dosimetry to be applied in precision medicine and personalized TRT.

Chapter 4. Conclusion

In this study, a preclinical image-based internal radiation dosimetry for diagnostic radiopharmaceuticals was developed, and the theranostic surrogacy of companion diagnostic radiopharmaceuticals for radionuclide therapy was investigated in terms of voxel-level dosimetry.

Preclinical dosimetry studies using disease animal models continue to gain interest as molecular imaging is applied in new domains, specifically as a standard theranostic tool for studying biodistribution, predicting clinical use, and radiological safety of novel biomolecules or molecular mechanisms. In Chapter 2, the image-based dosimetry method was successfully established at the organ-/voxel-level in the xenograft model mice for two prostate cancer diagnostic radiopharmaceuticals, which require sufficient preclinical studies. [^{68}Ga]PSMA-11 and [^{18}F]PSMA-1007 have already been adopted at several institutions worldwide and have become the most widely used for PET in clinical practice. Dosimetry at the voxel level was used to accurately determine the absorbed dose not only in major organs but also in abnormal tumors and dose-limiting critical organs, such as the salivary glands and kidneys. Assessing the dose distribution in the xenograft mice proved the value of preclinical evaluation for determining the clinical usefulness of these two diagnostic radiopharmaceuticals in the xenograft mice. A preclinical research paradigm showed great promise for use in patient-specific dosimetry, considering patient-specific heterogeneous tissue compositions and activity distributions.

The aim of TRT is to deliver the maximal dose to target tissues while minimizing dose-limiting adverse effects in off-target organs associated with

radiopharmaceuticals. Although TRT dosimetry-guided dose determination is theoretically optimal, poor imaging of non-less quantitative radionuclides makes it difficult to quantify heterogeneous inter-/intralesional uptake and inaccurate lesion masses. In Chapter 3, the use of imaging radionuclides-labeled surrogates was investigated, and the therapeutic absorbed doses for differentiated thyroid cancer therapy in xenograft model mice were discussed. The hypothetical energy deposition/dose distribution images were produced as [^{123}I]NaI SPECT by applying ^{131}I ion source simulation, and the investigated methodology of surrogates could be used for assessing the three-dimensional distribution of the absorbed dose for alpha- and/or beta-particle emitter-labeled therapeutics. Furthermore, a novel approach was proposed for simplifying voxel-level dosimetry, and an experimental basis was suggested for determining the minimal and optimal scan time points of surrogates for pretherapeutic dosimetry.

Finally, preclinical internal radiation dosimetry for optimizing radionuclide therapy was performed and investigated for the development of voxel-level dosimetry in a disease mouse model. Preclinical dosimetry can provide a starting point for the management of therapeutic strategies for promising radiopharmaceuticals and improving patient-specific treatment plans. Together with these results, it is expected to improve the challenging dosimetric process for clinical use and evaluation of the absorbed dose of target/off-target tissues more precisely.

Notes

Parts of Chapter 2 have been published as stated below.

Kim SB (Su Bin Kim), Song IH, Song YS, et al. Biodistribution and internal radiation dosimetry of a companion diagnostic radiopharmaceutical, [^{68}Ga]PSMA-11, in subcutaneous prostate cancer xenograft model mice. *Sci Rep*. 2021;11(1):15263. doi:10.1038/s41598-021-94684-6.

Kim SB (Su Bin Kim), Song IH, Kim SY, et al. Preclinical Evaluation of a Companion Diagnostic Radiopharmaceutical, [^{18}F]PSMA-1007, in a Subcutaneous Prostate Cancer Xenograft Mouse Model. *Mol Pharm*. Published online December 30, 2022. doi:10.1021/acs.molpharmaceut.2c00788.

References

1. Goldsmith SJ. Targeted radionuclide therapy: A historical and personal review. Semin Nucl Med. 2020;50(1):87-97. doi:10.1053/j.semnuclmed.2019.07.006

2. Gupta A, Lee MS, Kim JH, et al. Preclinical voxel-based dosimetry through GATE Monte Carlo simulation using PET/CT imaging of mice. Phys Med Biol. 2019;64(9):095007. doi:10.1088/1361-6560/ab134b

3. Gupta A, Shin JH, Lee MS, et al. Voxel-Based Dosimetry of Iron Oxide Nanoparticle-Conjugated 177Lu-Labeled Folic Acid Using SPECT/CT Imaging of Mice. Mol Pharm. 2019;16(4):1498-1506. doi:10.1021/acs.molpharmaceut.8b01125

4. Sgouros G, Frey E, Wahl R, He B, Prideaux A, Hobbs R. Three-dimensional imaging-based radiobiological dosimetry. Semin Nucl Med. 2008;38(5):321-334. doi:10.1053/j.semnuclmed.2008.05.008

5. Wahl RL, Sunderland J. Radiopharmaceutical dosimetry for cancer therapy: from theory to practice. J Nucl Med. 2021;62(Suppl 3):1S-2S. doi:10.2967/jnumed.121.263273

6. Malamud H. MIRD primer for absorbed dose calculations. Clin Nucl Med. 1989;14(9):723-724. doi:10.1097/00003072-198909000-00027

7. Segars WP, Tsui BMW, Frey EC, Johnson GA, Berr SS. Development of a 4-D digital mouse phantom for molecular imaging research. Mol Imaging Biol. 2004;6(3):149-159. doi:10.1016/j.mibio.2004.03.002

8. Stabin MG, Xu XG, Emmons MA, Segars WP, Shi C, Fernald MJ. RADAR reference adult, pediatric, and pregnant female phantom series for internal and external dosimetry. J Nucl Med. 2012;53(11):1807-1813.

doi:10.2967/jnumed.112.106138

9. Lee MS, Kim JH, Paeng JC, et al. Whole-Body Voxel-Based Personalized Dosimetry: The Multiple Voxel S-Value Approach for Heterogeneous Media with Nonuniform Activity Distributions. J Nucl Med. 2018;59(7):1133-1139. doi:10.2967/jnumed.117.201095

10. Stabin MG, Peterson TE, Holburn GE, Emmons MA. Voxel-based mouse and rat models for internal dose calculations. J Nucl Med. 2006;47(4):655-659.

11. Bitar A, Lisbona A, Thedrez P, et al. A voxel-based mouse for internal dose calculations using Monte Carlo simulations (MCNP). Phys Med Biol. 2007;52(4):1013-1025. doi:10.1088/0031-9155/52/4/010

12. Xie T, Zaidi H. Monte Carlo-based evaluation of S-values in mouse models for positron-emitting radionuclides. Phys Med Biol. 2013;58(1):169-182. doi:10.1088/0031-9155/58/1/169

13. Larsson E, Strand S-E, Ljungberg M, Jönsson B-A. Mouse S-factors based on Monte Carlo simulations in the anatomical realistic Moby phantom for internal dosimetry. Cancer Biother Radiopharm. 2007;22(3):438-442. doi:10.1089/cbr.2006.320

14. Buckley LA, Kawrakow I, Rogers DWO. An EGSnrc investigation of cavity theory for ion chambers measuring air kerma. Med Phys. 2003;30(6):1211-1218. doi:10.1118/1.1573891

15. Bednarz B, Grudzinski J, Marsh I, et al. Murine-specific Internal Dosimetry for Preclinical Investigations of Imaging and Therapeutic Agents. Health Phys. 2018;114(4):450-459. doi:10.1097/HP.0000000000000789

16. Pool SE, Krenning EP, Koning GA, et al. Preclinical and clinical studies of

peptide receptor radionuclide therapy. Semin Nucl Med. 2010;40(3):209-218. doi:10.1053/j.semnuclmed.2009.12.001

17. Dash A, Chakraborty S, Pillai MRA, Knapp FFR. Peptide receptor radionuclide therapy: an overview. Cancer Biother Radiopharm. 2015;30(2):47-71. doi:10.1089/cbr.2014.1741

18. Lawhn-Heath C, Hope TA, Martinez J, et al. Dosimetry in radionuclide therapy: the clinical role of measuring radiation dose. Lancet Oncol. 2022;23(2):e75-e87. doi:10.1016/S1470-2045(21)00657-4

19. Miller C, Rousseau J, Ramogida CF, Celler A, Rahmim A, Uribe CF. Implications of physics, chemistry and biology for dosimetry calculations using theranostic pairs. Theranostics. 2022;12(1):232-259. doi:10.7150/thno.62851

20. Redfern JS. Theranostics: Cancer imaging and therapy using injectable radionuclide-labeled ligands. PPIJ. 2020;8(6):325-331. doi:10.15406/ppij.2020.08.00313

21. Hänscheid H, Lapa C, Buck AK, Lassmann M, Werner RA. Dose Mapping After Endoradiotherapy with 177Lu-DOTATATE/DOTATOC by a Single Measurement After 4 Days. J Nucl Med. 2018;59(1):75-81. doi:10.2967/jnumed.117.193706

22. Madsen MT, Menda Y, O'Dorisio TM, O'Dorisio MS. Technical Note: Single time point dose estimate for exponential clearance. Med Phys. 2018;45(5):2318-2324. doi:10.1002/mp.12886

23. Hou X, Brosch J, Uribe C, et al. Feasibility of Single-Time-Point Dosimetry for Radiopharmaceutical Therapies. J Nucl Med. 2021;62(7):1006-1011. doi:10.2967/jnumed.120.254656

24. Willowson KP, Eslick E, Ryu H, Poon A, Bernard EJ, Bailey DL. Feasibility and

accuracy of single time point imaging for renal dosimetry following 177Lu-DOTATATE ('Lutate') therapy. EJNMMI Phys. 2018;5(1):33. doi:10.1186/s40658-018-0232-9

25. Devasia TP, Dewaraja YK, Frey KA, Wong KK, Schipper MJ. A Novel Time-Activity Information-Sharing Approach Using Nonlinear Mixed Models for Patient-Specific Dosimetry with Reduced Imaging Time Points: Application in SPECT/CT After 177Lu-DOTATATE. J Nucl Med. 2021;62(8):1118-1125. doi:10.2967/jnumed.120.256255

26. Ardenfors O, Nilsson JN, Thor D, Hindorf C. Simplified dosimetry for kidneys and tumors in 177Lu-labeled peptide receptor radionuclide therapy. EJNMMI Phys. 2022;9(1):44. doi:10.1186/s40658-022-00473-z

27. Silver DA, Pellicer I, Fair WR, Heston WD, Cordon-Cardo C. Prostate-specific membrane antigen expression in normal and malignant human tissues. Clin Cancer Res. 1997;3(1):81-85.

28. Eder M, Schäfer M, Bauder-Wüst U, et al. 68Ga-complex lipophilicity and the targeting property of a urea-based PSMA inhibitor for PET imaging. Bioconjug Chem. 2012;23(4):688-697. doi:10.1021/bc200279b

29. Afshar-Oromieh A, Holland-Letz T, Giesel FL, et al. Diagnostic performance of 68Ga-PSMA-11 (HBED-CC) PET/CT in patients with recurrent prostate cancer: evaluation in 1007 patients. Eur J Nucl Med Mol Imaging. 2017;44(8):1258-1268. doi:10.1007/s00259-017-3711-7

30. Hong J-J, Liu B, Wang Z-Q, et al. The value of 18F-PSMA-1007 PET/CT in identifying non-metastatic high-risk prostate cancer. EJNMMI Res. 2020;10(1):138. doi:10.1186/s13550-020-00730-1

31. Giesel FL, Hadaschik B, Cardinale J, et al. F-18 labelled PSMA-1007: biodistribution, radiation dosimetry and histopathological validation of tumor lesions in prostate cancer patients. Eur J Nucl Med Mol Imaging. 2017;44(4):678-688. doi:10.1007/s00259-016-3573-4

32. Kuten J, Fahoum I, Savin Z, et al. Head-to-Head Comparison of 68Ga-PSMA-11 with 18F-PSMA-1007 PET/CT in Staging Prostate Cancer Using Histopathology and Immunohistochemical Analysis as a Reference Standard. J Nucl Med. 2020;61(4):527-532. doi:10.2967/jnumed.119.234187

33. Sprute K, Kramer V, Koerber SA, et al. Diagnostic Accuracy of 18F-PSMA-1007 PET/CT Imaging for Lymph Node Staging of Prostate Carcinoma in Primary and Biochemical Recurrence. J Nucl Med. 2021;62(2):208-213. doi:10.2967/jnumed.120.246363

34. Cardinale J, Schäfer M, Benešová M, et al. Preclinical Evaluation of 18F-PSMA-1007, a New Prostate-Specific Membrane Antigen Ligand for Prostate Cancer Imaging. J Nucl Med. 2017;58(3):425-431. doi:10.2967/jnumed.116.181768

35. Kratochwil C, Giesel FL, Stefanova M, et al. PSMA-Targeted Radionuclide Therapy of Metastatic Castration-Resistant Prostate Cancer with 177Lu-Labeled PSMA-617. J Nucl Med. 2016;57(8):1170-1176. doi:10.2967/jnumed.115.171397

36. Giesel FL, Cardinale J, Schäfer M, et al. (18)F-Labelled PSMA-1007 shows similarity in structure, biodistribution and tumour uptake to the theragnostic compound PSMA-617. Eur J Nucl Med Mol Imaging. 2016;43(10):1929-1930. doi:10.1007/s00259-016-3447-9

37. Agostinelli S, Allison J, Amako K, et al. Geant4—a simulation toolkit. Nuclear Instruments and Methods in Physics Research Section A: Accelerators,

Spectrometers, Detectors and Associated Equipment. 2003;506(3):250-303. doi:10.1016/S0168-9002(03)01368-8

38. Perrot Y, Degoul F, Auzeloux P, et al. Internal dosimetry through GATE simulations of preclinical radiotherapy using a melanin-targeting ligand. Phys Med Biol. 2014;59(9):2183-2198. doi:10.1088/0031-9155/59/9/2183

39. Jabari M, Rajabi H, Dadashzadeh S. A microdosimetry model of kidney by GATE Monte Carlo simulation using a nonuniform activity distribution in digital phantom of nephron. Nucl Med Commun. 2020;41(2):110-119. doi:10.1097/MNM.0000000000001112

40. Thiam CO, Breton V, Donnarieix D, Habib B, Maigne L. Validation of a dose deposited by low-energy photons using GATE/GEANT4. Phys Med Biol. 2008;53(11):3039-3055. doi:10.1088/0031-9155/53/11/019

41. Grevillot L, Bertrand D, Dessy F, Freud N, Sarrut D. A Monte Carlo pencil beam scanning model for proton treatment plan simulation using GATE/GEANT4. Phys Med Biol. 2011;56(16):5203-5219. doi:10.1088/0031-9155/56/16/008

42. Kost SD, Dewaraja YK, Abramson RG, Stabin MG. VIDA: a voxel-based dosimetry method for targeted radionuclide therapy using Geant4. Cancer Biother Radiopharm. 2015;30(1):16-26. doi:10.1089/cbr.2014.1713

43. Sarrut D, Bardiès M, Boussion N, et al. A review of the use and potential of the GATE Monte Carlo simulation code for radiation therapy and dosimetry applications. Med Phys. 2014;41(6):064301. doi:10.1118/1.4871617

44. Kostou T, Papadimitroulas P, Loudos G, Kagadis GC. A preclinical simulated dataset of S-values and investigation of the impact of rescaled organ masses using the MOBY phantom. Phys Med Biol. 2016;61(6):2333-2355. doi:10.1088/0031-

9155/61/6/2333

45. Boutaleb S, Pouget JP, Hindorf C, et al. Impact of mouse model on preclinical dosimetry in targeted radionuclide therapy. Proc IEEE. 2009;97(12):2076-2085. doi:10.1109/JPROC.2009.2026921

46. Matsumoto M, Nishimura T. Mersenne twister: a 623-dimensionally equidistributed uniform pseudo-random number generator. ACM Trans Model Comput Simul. 1998;8(1):3-30. doi:10.1145/272991.272995

47. Andersson M, Johansson L, Eckerman K, Mattsson S. IDAC-Dose 2.1, an internal dosimetry program for diagnostic nuclear medicine based on the ICRP adult reference voxel phantoms. EJNMMI Res. 2017;7(1):88. doi:10.1186/s13550-017-0339-3

48. Stabin MG, Konijnenberg MW. Re-evaluation of absorbed fractions for photons and electrons in spheres of various sizes. J Nucl Med. 2000;41(1):149-160.

49. Stabin MG, Sparks RB, Crowe E. OLINDA/EXM: the second-generation personal computer software for internal dose assessment in nuclear medicine. J Nucl Med. 2005;46(6):1023-1027.

50. Constantinescu CC, Sevrioukov E, Garcia A, Pan M-L, Mukherjee J. Evaluation of [18F]Mefway biodistribution and dosimetry based on whole-body PET imaging of mice. Mol Imaging Biol. 2013;15(2):222-229. doi:10.1007/s11307-012-0582-y

51. Keenan MA, Stabin MG, Segars WP, Fernald MJ. RADAR realistic animal model series for dose assessment. J Nucl Med. 2010;51(3):471-476. doi:10.2967/jnumed.109.070532

52. Menzel H-G, Clement C, DeLuca P. ICRP Publication 110. Realistic reference phantoms: an ICRP/ICRU joint effort. A report of adult reference computational

phantoms. Ann ICRP. 2009;39(2):1-164. doi:10.1016/j.icrp.2009.09.001

53. Cristy M, Eckerman KF. Specific Absorbed Fractions of Energy at Various Ages from Internal Photon Sources: 7, Adult Male. Oak Ridge National Laboratory (ORNL); 1987. doi:10.2172/6233638

54. Garrow AA, Andrews JPM, Gonzalez ZN, et al. Preclinical dosimetry models and the prediction of clinical doses of novel positron emission tomography radiotracers. Sci Rep. 2020;10(1):15985. doi:10.1038/s41598-020-72830-w

55. Cardinale J, Martin R, Remde Y, et al. Procedures for the GMP-Compliant Production and Quality Control of [18F]PSMA-1007: A Next Generation Radiofluorinated Tracer for the Detection of Prostate Cancer. Pharmaceuticals (Basel). 2017;10(4). doi:10.3390/ph10040077

56. European Pharmacopoeia (Ph. Eur.) 10th Edition - European Directorate for the Quality of Medicines & HealthCare. Accessed August 7, 2022. https://www.edqm.eu/en/web/edqm/european-pharmacopoeia-ph-eur-10th-edition

57. Buckeridge C, Duvvuri S, Denney WS. Simple, automatic noncompartmental analysis: the PKNCA R package. J Pharmacokinet Pharmacodyn. 2015;42(1):11-107.

58. Jaki T, Wolfsegger MJ. Estimation of pharmacokinetic parameters with the R package PK. Pharm Stat. 2011;10(3):284-288. doi:10.1002/pst.449

59. Sachpekidis C, Afshar-Oromieh A, Kopka K, et al. 18F-PSMA-1007 multiparametric, dynamic PET/CT in biochemical relapse and progression of prostate cancer. Eur J Nucl Med Mol Imaging. 2020;47(3):592-602. doi:10.1007/s00259-019-04569-0

60. McDermott S, Yan D. WE-C-217BCD-12: Irreversible Two-Tissue

Compartment Model Fitting for Dynamic 18F- FDG PET: A Practical Comparison of Methods Using Simulated Time- Activity Data. Med Phys. 2012;39(6Part27):3952. doi:10.1118/1.4736128

61. Baumgartner R, Joshi A, Feng D, Zanderigo F, Ogden RT. Statistical evaluation of test-retest studies in PET brain imaging. EJNMMI Res. 2018;8(1):13. doi:10.1186/s13550-018-0366-8

62. Hillier SM, Maresca KP, Femia FJ, et al. Preclinical evaluation of novel glutamate-urea-lysine analogues that target prostate-specific membrane antigen as molecular imaging pharmaceuticals for prostate cancer. Cancer Res. 2009;69(17):6932-6940. doi:10.1158/0008-5472.CAN-09-1682

63. Afshar-Oromieh A, Hetzheim H, Kübler W, et al. Radiation dosimetry of (68)Ga-PSMA-11 (HBED-CC) and preliminary evaluation of optimal imaging timing. Eur J Nucl Med Mol Imaging. 2016;43(9):1611-1620. doi:10.1007/s00259-016-3419-0

64. Soeda F, Watabe T, Naka S, et al. Impact of 18F-PSMA-1007 Uptake in Prostate Cancer Using Different Peptide Concentrations: Preclinical PET/CT Study on Mice. J Nucl Med. 2019;60(11):1594-1599. doi:10.2967/jnumed.118.223479

65. Heynickx N, Herrmann K, Vermeulen K, Baatout S, Aerts A. The salivary glands as a dose limiting organ of PSMA- targeted radionuclide therapy: A review of the lessons learnt so far. Nucl Med Biol. 2021;98-99:30-39. doi:10.1016/j.nucmedbio.2021.04.003

66. Peters SMB, Hofferber R, Privé BM, et al. [68Ga]PSMA-11 PET imaging as a predictor for absorbed doses in organs at risk and small lesions in [177Lu]PSMA-617 treatment. Eur J Nucl Med Mol Imaging. 2022;49(4):1101-1112. doi:10.1007/s00259-021-05538-2

67. Yadav MP, Ballal S, Sahoo RK, Bal C. Efficacy and safety of 225Ac-DOTATATE targeted alpha therapy in metastatic paragangliomas: a pilot study. Eur J Nucl Med Mol Imaging. 2022;49(5):1595-1606. doi:10.1007/s00259-021-05632-5

68. Nakata N, Kobashi N, Okumura Y, et al. Radiation dosimetry and efficacy of an 89Zr/225Ac-labeled humanized anti-MUC5AC antibody. Nucl Med Biol. 2022;108-109:33-43. doi:10.1016/j.nucmedbio.2022.02.003

69. Kelly VJ, Wu S-T, Gottumukkala V, et al. Preclinical evaluation of an 111In/225Ac theranostic targeting transformed MUC1 for triple negative breast cancer. Theranostics. 2020;10(15):6946-6958. doi:10.7150/thno.38236

70. Morari EC, Marcello MA, Guilhen ACT, et al. Use of sodium iodide symporter expression in differentiated thyroid carcinomas. Clin Endocrinol (Oxf). 2011;75(2):247-254. doi:10.1111/j.1365-2265.2011.04032.x

71. Tavares C, Coelho MJ, Eloy C, et al. NIS expression in thyroid tumors, relation with prognosis clinicopathological and molecular features. Endocr Connect. 2018;7(1):78-90. doi:10.1530/EC-17-0302

72. Benua RS, Cicale NR, Sonenberg M, Rawson RW. The relation of radioiodine dosimetry to results and complications in the treatment of metastatic thyroid cancer. Am J Roentgenol Radium Ther Nucl Med. 1962;87:171-182.

73. Hänscheid H, Canzi C, Eschner W, et al. EANM Dosimetry Committee series on standard operational procedures for pre-therapeutic dosimetry II. Dosimetry prior to radioiodine therapy of benign thyroid diseases. Eur J Nucl Med Mol Imaging. 2013;40(7):1126-1134. doi:10.1007/s00259-013-2387-x

74. Ciarallo A, Rivera J. Radioactive iodine therapy in differentiated thyroid cancer: 2020 update. AJR Am J Roentgenol. 2020;215(2):285-291.

doi:10.2214/AJR.19.22626

75. Klubo-Gwiezdzinska J, Van Nostrand D, Atkins F, et al. Efficacy of dosimetric versus empiric prescribed activity of 131I for therapy of differentiated thyroid cancer. J Clin Endocrinol Metab. 2011;96(10):3217-3225. doi:10.1210/jc.2011-0494

76. Maxon HR, Englaro EE, Thomas SR, et al. Radioiodine-131 therapy for well-differentiated thyroid cancer--a quantitative radiation dosimetric approach: outcome and validation in 85 patients. J Nucl Med. 1992;33(6):1132-1136.

77. Pandit-Taskar N, Iravani A, Lee D, et al. Dosimetry in clinical radiopharmaceutical therapy of cancer: practicality versus perfection in current practice. J Nucl Med. 2021;62(Suppl 3):60S-72S. doi:10.2967/jnumed.121.262977

78. Van Nostrand D, Atkins F, Yeganeh F, Acio E, Bursaw R, Wartofsky L. Dosimetrically determined doses of radioiodine for the treatment of metastatic thyroid carcinoma. Thyroid. 2002;12(2):121-134. doi:10.1089/105072502753522356

79. de Keizer B, Brans B, Hoekstra A, et al. Tumour dosimetry and response in patients with metastatic differentiated thyroid cancer using recombinant human thyrotropin before radioiodine therapy. Eur J Nucl Med Mol Imaging. 2003;30(3):367-373. doi:10.1007/s00259-002-1076-y

80. Lee YS, Kim JS, Cho KD, Kang JH, Lim SM. Tumor dosimetry for I-131 trastuzumab therapy in a Her2+ NCI N87 xenograft mouse model using the Siemens SYMBIA E gamma camera with a pinhole collimator. J Inst. 2015;10(07):P07001-P07001. doi:10.1088/1748-0221/10/07/P07001

81. Rösch F, Herzog H, Qaim SM. The beginning and development of the theranostic approach in nuclear medicine, as exemplified by the radionuclide pair 86Y and 90Y.

Pharmaceuticals (Basel). 2017;10(2). doi:10.3390/ph10020056

82. Förster GJ, Engelbach MJ, Brockmann JJ, et al. Preliminary data on biodistribution and dosimetry for therapy planning of somatostatin receptor positive tumours: comparison of (86)Y-DOTATOC and (111)In-DTPA-octreotide. Eur J Nucl Med. 2001;28(12):1743-1750. doi:10.1007/s002590100628

83. Dalm SU, Bakker IL, de Blois E, et al. 68Ga/177Lu-NeoBOMB1, a Novel Radiolabeled GRPR Antagonist for Theranostic Use in Oncology. J Nucl Med. 2017;58(2):293-299. doi:10.2967/jnumed.116.176636

84. Kolbert KS, Pentlow KS, Pearson JR, et al. Prediction of absorbed dose to normal organs in thyroid cancer patients treated with 131I by use of 124I PET and 3-dimensional internal dosimetry software. J Nucl Med. 2007;48(1):143-149.

85. Sgouros G, Kolbert KS, Sheikh A, et al. Patient-specific dosimetry for 131I thyroid cancer therapy using 124I PET and 3-dimensional-internal dosimetry (3D-ID) software. J Nucl Med. 2004;45(8):1366-1372.

86. Kuker R, Sztejnberg M, Gulec S. I-124 Imaging and Dosimetry. Mol Imaging Radionucl Ther. 2017;26(Suppl 1):66-73. doi:10.4274/2017.26.suppl.07

87. Conti M, Eriksson L. Physics of pure and non-pure positron emitters for PET: a review and a discussion. EJNMMI Phys. 2016;3(1):8. doi:10.1186/s40658-016-0144-5

88. Simplified Dosimetry Methods in Thyroid Cancer: An Overview of Methods that Can Be Implemented in Clinical Practice for Treatment Planning with I-131 | Journal of Nuclear Medicine. Accessed December 15, 2022. https://jnm.snmjournals.org/content/61/supplement_1/1187/tab-article-info

89. Maaß C, Sachs JP, Hardiansyah D, Mottaghy FM, Kletting P, Glatting G.

Dependence of treatment planning accuracy in peptide receptor radionuclide therapy on the sampling schedule. EJNMMI Res. 2016;6(1):30. doi:10.1186/s13550-016-0185-8

90. Sandström M, Freedman N, Fröss-Baron K, Kahn T, Sundin A. Kidney dosimetry in 777 patients during 177Lu-DOTATATE therapy: aspects on extrapolations and measurement time points. EJNMMI Phys. 2020;7(1):73. doi:10.1186/s40658-020-00339-2

91. Sundlöv A, Gustafsson J, Brolin G, et al. Feasibility of simplifying renal dosimetry in 177Lu peptide receptor radionuclide therapy. EJNMMI Phys. 2018;5(1):12. doi:10.1186/s40658-018-0210-2

92. Sisson JC, Shulkin BL, Lawson S. Increasing efficacy and safety of treatments of patients with well-differentiated thyroid carcinoma by measuring body retentions of 131I. J Nucl Med. 2003;44(6):898-903.

93. Traino AC, Di Martino F, Boni G, Mariani G, Lazzeri M. A minimally invasive method to evaluate 131I kinetics in blood. Radiat Prot Dosimetry. 2004;109(3):249-252. doi:10.1093/rpd/nch041

94. Van Nostrand D, Atkins F, Moreau S, et al. Utility of the radioiodine whole-body retention at 48 hours for modifying empiric activity of 131-iodine for the treatment of metastatic well-differentiated thyroid carcinoma. Thyroid. 2009;19(10):1093-1098. doi:10.1089/thy.2008.0339

95. Atkins FB, Van Nostrand D. Simplified methods of dosimetry. In: Wartofsky L, Van Nostrand D, eds. Thyroid Cancer. Springer New York; 2016:651-656. doi:10.1007/978-1-4939-3314-3_59

96. Dohán O, De la Vieja A, Paroder V, et al. The sodium/iodide Symporter (NIS):

characterization, regulation, and medical significance. Endocr Rev. 2003;24(1):48-77. doi:10.1210/er.2001-0029

97. Spetz J, Rudqvist N, Forssell-Aronsson E. Biodistribution and dosimetry of free 211At, 125I- and 131I- in rats. Cancer Biother Radiopharm. 2013;28(9):657-664. doi:10.1089/cbr.2013.1483

98. Walker RC, Smith GT, Liu E, Moore B, Clanton J, Stabin M. Measured human dosimetry of 68Ga-DOTATATE. J Nucl Med. 2013;54(6):855-860. doi:10.2967/jnumed.112.114165

99. Nedrow JR, Josefsson A, Park S, et al. Pharmacokinetics, microscale distribution, and dosimetry of alpha-emitter-labeled anti-PD-L1 antibodies in an immune competent transgenic breast cancer model. EJNMMI Res. 2017;7(1):57. doi:10.1186/s13550-017-0303-2

100. Weineisen M, Schottelius M, Simecek J, et al. 68Ga- and 177Lu-Labeled PSMA I&T: Optimization of a PSMA-Targeted Theranostic Concept and First Proof-of-Concept Human Studies. J Nucl Med. 2015;56(8):1169-1176. doi:10.2967/jnumed.115.158550

101. Maffey-Steffan J, Scarpa L, Svirydenka A, et al. The 68Ga/177Lu-theragnostic concept in PSMA-targeting of metastatic castration-resistant prostate cancer: impact of post-therapeutic whole-body scintigraphy in the follow-up. Eur J Nucl Med Mol Imaging. 2020;47(3):695-712. doi:10.1007/s00259-019-04583-2

102. Chicheportiche A, Ben-Haim S, Grozinsky-Glasberg S, et al. Dosimetry after peptide receptor radionuclide therapy: impact of reduced number of post-treatment studies on absorbed dose calculation and on patient management. EJNMMI Phys. 2020;7(1):5. doi:10.1186/s40658-020-0273-8

103. Heikkonen J, Mäenpää H, Hippeläinen E, Reijonen V, Tenhunen M. Effect of calculation method on kidney dosimetry in 177Lu-octreotate treatment. Acta Oncol. 2016;55(9-10):1069-1076. doi:10.1080/0284186X.2016.1182642

104. Rinscheid A, Kletting P, Eiber M, Beer AJ, Glatting G. Influence of sampling schedules on [177Lu]Lu-PSMA dosimetry. EJNMMI Phys. 2020;7(1):41. doi:10.1186/s40658-020-00311-0

국문초록

정밀 방사성 핵종 치료를 위한 전임상 내부 흡수선량평가 연구

개인 맞춤형 의료와 표적 방사성 핵종 치료에 대한 관심이 높아짐에 따라 내부 흡수선량평가는 최근 몇 년 동안 더욱 중요해졌다. 특히 질병 모델 동물을 이용한 전임상 흡수선량평가는 새로운 테라노스직스 의약품의 분포를 연구하거나 모든 환자에게 동일 용량이 투여되는 기존의 방사선치료전략을 개선하는데 유망한 기술로써 관심이 계속해서 높아지고 있다. 정밀한 전임상 흡수선량이 반응 평가를 위한 선량 분포를 이해하고 임상에서의 활용을 위한 중개 연구서 중요하지만, 정량적으로 이미지화 되기 어려운 알파나 베타 입자를 방출하는 동위원소를 포함하여 치료용 방사성의약품의 용량을 결정하거나, 동반 진단용약물의 외삽 전략에 관한 연구가 충분하지 않다.

제2장에서는, 이종이식 마우스 모델을 이용한 진단용 방사성의약품의 영상 기반 흡수선량평가 방법의 개발이다. 임상적으로 흡수선량평가에 승인을 받은 방법은 MIRD (Medical Internal Radiation Dosimetry) 위원회에서 권장되어 왔다. 장기 수준에서 평가하는 표준화된 흡수선량평가 방법이 일반화된 형식을 사용한다 할지라도, 각

종(species)의 표준화된 대표 모델은 대상의 크기, 모양, 조직의 이질성을 대표할 수 있을 만큼 견고하지 않다. 그의 대안으로 복셀을 기반으로 한 흡수선량평가는 방사능붕괴과정에 포함된 모든 이벤트를 시뮬레이션하는 몬테카를로 접근법을 통해 기존의 한계점을 극복하기 위해 개발되어 왔다.

전립선암 진단에 탁월한 두 진단용 방사성의약품–[^{68}Ga]PSMA-11 [^{18}F]PSMA-1007–을 전립선암 질환모델에 투여하여 장기 수준 및 복셀 수준에서 흡수선량을 평가했다. 복셀 수준은 종양과 같은 해부학적으로 일반적이지 않은 장기에서도 평가될 수 있고, 표준화된 팬텀의 한계를 극복할 수 있기에 더 실제와 가까운 결과를 생산할 수 있다. 마지막으로는 종양 모델에서의 데이터를 바탕으로 인체에서 흡수선량을 예측해 실제 데이터와 비교했다.

제3장에서는, 방사성 핵종 치료를 위한 동반 진단용 방사성의약품의 대리성을 복셀 수준 흡수선량평가 방법론을 적용하고 표적 방사성 핵종 치료에서 최소의 영상 획득 시점을 이용한 선량 측정 방법을 발전시키기 위한 전임상 연구의 패러다임을 입증하는 것이다. 분화갑상선암 (DTC) 이종이식 모델 마우스의 개체 특이적인 복셀화된-팬텀/소스 이미지가 사용되었으며, [^{123}I]NaI SPECT/CT 영상으로부터 I-131 치료를 위한 에너지 축적 맵 (E_{dep} map) 과 선량 분포 맵 (Dose map) 을 만들어냈다. 몬테카를로 시뮬레이션으로 [^{131}I]NaI에 대한 외삽된 선량률 곡선을 사용하여 복셀 수준에서 단순화된 흡수선량 방법론을 구상했다. 반감기

차이가 큰 치료 방사성 의약품의 생체 분포를 포착할 수 있고 최소한의 동반 진단용 방사성의약품 영상으로도 흡수선량을 평가하여 환자와 의료인의 피로도가 큰 흡수선량 과정을 단순화 하는 방법 개발이 목표이다. 기존의 장기 수준에서 복셀 수준으로 관점을 확대한 측면에서 개인의 조직특이성 및 약물 분포 이질성을 고려한 단순화된 흡수선량 방법이라고 할 수 있으며, 이는 임상 적용의 기초 데이터로 활용될 수 있을 것이다.

치료 전 환자 개인별 흡수선량평가는 다양한 암의 표적 방사성 핵종 치료의 계획에서 중요한 역할을 하여 종양 조절 가능성을 높이고 정상 조직 독성을 감소시킨다. 또한, 전임상 내부 방사선량 측정은 투여 용량 결정 및 치료 효능 평가를 최적화하기 위한 중개 연구 측면에서 큰 가치가 있다. 본 학위 논문에서 몬테카를로 시뮬레이션을 이용한 접근 방식은 유망한 방사성 의약품의 치료 전략을 관리하고 환자 개인별 치료 계획을 개선하기 위한 기초 자료를 제공할 것으로 기대된다.

주요어: 전임상 흡수선량평가, 몬테카를로 시뮬레이션, 표적 방사성 핵종 치료, 맞춤 의학, 테라노스틱스

학 번: 2019-25365